# Multi-color fluorescence fluctuation spectroscopy in living cells via spectral detection

Valentin Dunsing*, Annett Petrich and Salvatore Chiantia*

University of Potsdam, Institute of Biochemistry and Biology, Karl-Liebknecht-Str. 24-25, 14476 Potsdam, Germany

*To whom correspondence should be addressed: dunsing@uni-potsdam.de, chiantia@uni-potsdam.de

## Abstract:

Signaling pathways in biological systems rely on specific interactions between multiple biomolecules. Fluorescence fluctuation spectroscopy provides a powerful toolbox to quantify such interactions directly in living cells. Cross-correlation analysis of spectrally separated fluctuations provides information about inter-molecular interactions but is usually limited to two fluorophore species. Here, we present scanning fluorescence spectral correlation spectroscopy (SFSCS), a versatile approach that can be implemented on commercial confocal microscopes, allowing the investigation of interactions between multiple protein species at the plasma membrane. We demonstrate that SFSCS enables cross-talk-free cross-correlation, diffusion and oligomerization analysis of up to four protein species labeled with strongly overlapping fluorophores. As an example, we investigate the interactions of influenza A virus (IAV) matrix protein 2 with two cellular host factors simultaneously. We furthermore apply raster spectral image correlation spectroscopy for the simultaneous analysis of up to four species and determine the stoichiometry of ternary IAV polymerase complexes in the cell nucleus.

**Abbreviations**

ACF, autocorrelation function; CCF, cross-correlation function; CF, correlation function; D, diffusion coefficient; F(C)CS, fluorescence (cross-) correlation spectroscopy; FFS,

fluorescence fluctuation spectroscopy; (sc-)FL(C)CS, (single-color) fluorescence lifetime (cross-) correlation spectroscopy; FP, fluorescent protein; FRET, fluorescence resonance energy transfer; FSCS, fluorescence spectral correlation spectroscopy; IAV, influenza A virus; M1, IAV matrix protein 1, M2, IAV matrix protein 2; mEGFP, monomeric enhanced green fluorescent protein; mEYFP, monomeric enhanced yellow fluorescent protein; mp, myristoylated and palmitoylated; HA, IAV hemagglutinin protein; PA, polymerase acidic protein; PB1/PB2, polymerase basic protein 1/2; PC, polymerase complex; $p_f$, fluorescence probability; PM, plasma membrane; RI(C)CS, raster image (cross-) correlation spectroscopy; ROI, region of interest; RSICS, raster spectral image correlation spectroscopy; SD, standard deviation; SF(C)CS, scanning fluorescence (cross-) correlation spectroscopy; SNR, signal-to-noise ratio; TRICS, triple raster image correlation spectroscopy

49 **INTRODUCTION**

50 Living cells rely on transport and interaction of biomolecules to perform their diverse functions.
51 To investigate the underlying molecular processes in the native cellular environment, minimally
52 invasive techniques are needed. Fluorescence fluctuation spectroscopy (FFS) approaches
53 provide a powerful toolbox that fulfills this aim (1–3). FFS takes advantage of inherent
54 molecular dynamics present in biological systems, for example diffusion, to obtain molecular
55 parameters from fluctuations of the signal emitted by an ensemble of fluorescent molecules.
56 More in detail, the temporal evolution of such fluctuations allows the quantification of
57 intracellular dynamics. In addition, concentration and oligomerization state of molecular
58 complexes can be determined by analyzing the magnitude of fluctuations. Finally, hetero-
59 interactions of different molecular species can be detected by cross-correlation analysis of
60 fluctuations emitted by spectrally separated fluorophores (4). Over the last two decades, several
61 experimental FFS schemes such as raster image (cross-) correlation spectroscopy (RI(C)CS)
62 (5, 6), (cross-correlation) Number&Brightness analysis (7, 8), and imaging FCS (9) have been
63 developed, extending the concept of traditional single-point fluorescence (cross-) correlation
64 spectroscopy (F(C)CS) (10). A further interesting example of FFS analysis relevant in the field
65 of cell biology is represented by scanning F(C)CS (SF(C)CS). Using a scanning path
66 perpendicular to the plasma membrane (PM), this technique provides enhanced stability and
67 the ability to probe slow membrane dynamics (11), protein interactions (12, 13) and
68 oligomerization (14) at the PM of cells.

69 FFS studies are conventionally limited to the analysis of two spectrally distinguished species,
70 due to i) broad emission spectra of fluorophores with consequent cross-talk artefacts, and ii)
71 limited overlap of detection/excitation geometries for labels with large spectral separation.
72 Generally, only few fluorescence-based methods are available to detect ternary or higher order
73 interactions of proteins (15–17). First *in vitro* approaches to perform FCS on more than two

74 species exploited different Stokes shifts of quantum dots (18) or fluorescent dyes excited with
75 a single laser line (19) or two-photon excitation (20, 21), coupled with detection on two or more
76 single photon counting detectors. Following an alternative conceptual approach, it was shown
77 *in vitro* that two spectrally strongly overlapping fluorophore species can be discriminated in
78 FCS by applying statistical filtering of detected photons based on spectrally resolved
79 (fluorescence spectral correlation spectroscopy, FSCS (22)) or fluorescence lifetime
80 (fluorescence lifetime correlation spectroscopy, FLCS (23–25)) detection. Such a framework
81 allows the minimization of cross-talk artefacts in FCCS measurements performed in living cells
82 (26). Recently, three-species implementations of RICCS and FCCS were successfully
83 demonstrated for the first time in living cells. Schrimpf et al. presented raster spectral image
84 correlation spectroscopy (RSICS), a powerful combination of RICS with spectral detection and
85 statistical filtering based on the emission spectra of mEGFP, mVenus and mCherry
86 fluorophores (27). Stefl et al. developed single-color fluorescence lifetime cross-correlation
87 spectroscopy (sc-FLCCS), taking advantage of several GFP variants characterized by short or
88 long fluorescence lifetimes (28). Using this elegant approach, three-species FCCS
89 measurements could be performed in yeast cells, with just two excitation lines.
90 Here, we explore the full potential of FSCS and RSICS. In particular, we present scanning
91 fluorescence spectral correlation spectroscopy (SFSCS), combining SFCS and FSCS. We show
92 that SFSCS enables cross-talk-free SFCCS measurements of two protein species at the PM of
93 living cells tagged with strongly overlapping fluorophores in the green or red region of the
94 visible spectrum, excited with a single excitation line. This approach results in correct estimates
95 of protein diffusion dynamics, oligomerization, and interactions between both species. Further,
96 we extend our approach to the analysis of three or four interacting partners: by performing
97 cross-correlation measurements on different fluorescent protein (FP) hetero-oligomers, we
98 demonstrate that up to four FP species can be simultaneously analyzed. We then apply this
99 scheme to simultaneously investigate the interaction of influenza A virus (IAV) matrix protein

100 2 (M2) with two cellular host factors, the tetraspanin CD9 and the autophagosome protein LC3,
101 co-expressed in the same cell. Finally, we extend RSICS for the detection of four molecular
102 species and quantify, for the first time directly in living cells, the complete stoichiometry of
103 ternary IAV polymerase complexes assembling in the nucleus, using three-species fluorescence
104 correlation and brightness analysis.
105
106
107

108 # RESULTS

109 **Cross-talk-free scanning SFSCS analysis of membrane-associated proteins using FPs with**
110 **strongly overlapping emission spectra and a single excitation wavelength**

111 To test the suitability of SFSCS to quantify interactions between membrane proteins tagged
112 with strongly spectrally overlapping fluorophores, we investigated HEK 293T cells co-
113 expressing mp-mEGFP and mp-mEYFP. These monomeric FPs are anchored independently to
114 the inner leaflet of the PM and their emission maxima are only ca. 20 nm apart (Figure 1-figure
115 supplement 1). The signal originating from the two fluorophores was decomposed using
116 spectral filters (Figure 1-figure supplement 2A) based on the emission spectra detected on cells
117 expressing mp-mEGFP and mp-mEYFP separately (Figure 1-figure supplement 1). We then
118 calculated autocorrelation functions (ACFs) and the cross-correlation function (CCF) for signal
119 fluctuations assigned to each fluorophore species. Representative CFs for a typical
120 measurement are shown in Fig.1A, indicating absence of interactions and negligible cross-talk
121 between the two FPs. In contrast, we observed substantial CCFs when analyzing measurements
122 on cells expressing mp-mEYFP-mEGFP hetero-dimers (Figure 1-figure supplement 3A).
123 Overall, we obtained a relative cross-correlation (rel.cc.) of 0.72±0.12 (mean±SD, n=22 cells)
124 in the latter sample, compared to a vanishing rel.cc. of 0.02±0.04 (mean±SD, n=34 cells) in the
125 negative control (Fig.1B). Comparison of two types of linker peptides (short flexible or long
126 rigid) between mEGFP and mEYFP showed that the linker length slightly affected rel.cc. values
127 obtained on hetero-dimers (Figure 1-figure supplement 3C). FPs linked by a short peptide
128 displayed lower rel.cc., probably due to fluorescence resonance energy transfer (FRET), as
129 previously reported (29). Therefore, unless otherwise noted, similar long rigid linkers were
130 inserted in all constructs used in this study that contain multiple FPs (see supplementary file
131 1a).

132 Overlapping fluorescence emission from different species detected in the same channels
133 provides unwanted background signal and thus reduces the signal-to-noise ratio (SNR) of the
134 CFs (27). To assess to which extent the SNR depends on the relative concentration of mEGFP
135 and mEYFP fluorophores, we compared it between measurements on cells with different
136 relative expression levels of the two membrane constructs (Fig.1C). While the SNR of mEGFP
137 ACFs was only moderately affected by the presence of mEYFP signal (i.e. SNR ranging from
138 ca. 2.5 to 1.0, with 90% to 10% of the signal originating from mEGFP), the ACFs measured
139 for mEYFP showed strong noise when mEGFP was present in much higher amount (i.e. SNR
140 ranging from 2.5 to 0.2, with 90% to 10% of the signal originating from mEYFP).
141 Next, we tested whether the same approach can be used for FPs with overlapping emission in
142 the red region of the visible spectrum, which generally suffer from reduced SNR in FFS
143 applications (14, 30). Therefore, we performed SFSCS measurements on HEK 293T cells co-
144 expressing mp-mCherry2 and mp-mApple. Also the emission spectra of these FPs are shifted
145 by less than 20 nm (Figure 1-figure supplement 1, spectral filters are shown in Figure 1-figure
146 supplement 2B). Correlation analysis resulted generally in noisier CFs (Fig.1D) compared to
147 mEGFP and mEYFP. Nevertheless, a consistently negligible rel.cc. of 0.04±0.06 (mean±SD,
148 n=24 cells) was observed. In contrast, a high rel.cc. of 0.78±0.19 (mean±SD, n=18 cells) was
149 obtained on cells expressing mp-mCherry2-mApple hetero-dimers (Fig.1E, Figure 1-figure
150 supplement 3B). SNR analysis confirmed lower SNRs of the CFs obtained for red FPs (Fig.1F)
151 compared to mEGFP and mEYFP, with mApple depending more weakly on the relative
152 fluorescence signal than mCherry2 (i.e. ca. 2-fold change for mApple vs. ca. 4-fold change for
153 mCherry2, when the relative abundance changed from 90% to 10%).
154

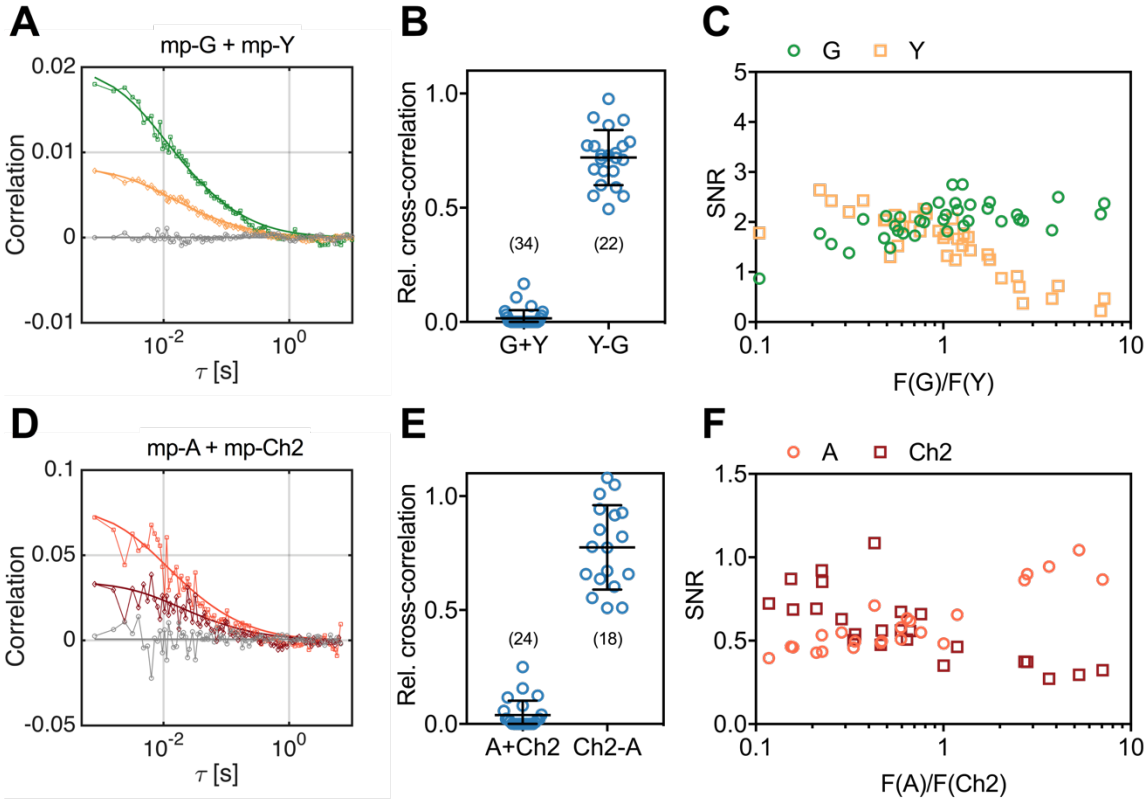


**Figure 1. Cross-correlation and SNR analysis for two-species SFSCS measurements at the PM of HEK 293T cells, performed with FPs showing strongly overlapping emission spectra. (A)** Representative CFs (green: ACF for mEGFP ("G"), yellow: ACF for mEYFP ("Y"), grey: CCF calculated for both fluorophore species) obtained from SFSCS measurements on the PM of HEK 293T cells co-expressing mp-mEGFP and mp-mEYFP. Solid thick lines show fits of a two-dimensional diffusion model to the CFs. **(B)** Relative cross-correlation values obtained from SFSCS measurements described in (A) ("G+Y") or on HEK 293T cells expressing mp-mEYFP-mEGFP hetero-dimers ("Y-G"). **(C)** SNR of ACFs for mEGFP (green) and mEYFP (yellow), obtained from SFSCS measurements described in (A), plotted as a function of the average ratio of detected mEGFP and mEYFP fluorescence. **(D)** Representative CFs (light red: ACF for mApple ("A"), dark red: ACF for mCherry2 ("Ch2"), grey: CCF calculated for both fluorophores) obtained from SFSCS measurements on the PM of HEK 293T cells co-expressing mp-mApple and mp-mCherry2. Solid thick lines show fits of a two-dimensional diffusion model to the CFs. **(E)** Relative cross-correlation values obtained from SFSCS measurements described in (D) ("A+Ch2") or on HEK 293T cells expressing mp-mCherry2-mApple hetero-dimers ("Ch2-A"). **(F)** SNR of ACFs for mApple (light red) and mCherry2 (dark red), obtained from SFSCS measurements described in (D), plotted as a function of the average ratio of detected mApple and mCherry2 fluorescence. Data are pooled from three (B) or two (E) independent experiments each. The number of cells measured is given in parentheses. Error bars represent mean±SD.

**Figure 1-figure supplement 1. FP emission spectra.** Average emission spectra of mp-mEGFP, mp-mEYFP, mp-mApple, mp-mCherry2 measured by spectral imaging (23 spectral channels from 491 nm to 695 nm) with 488 nm and 561 nm excitation on HEK 293T cells expressing each FP individually. Spectra are shown for two different days (day1: solid line, day2: dotted line) and averaged over four cells each. For each cell, 25 frames were acquired and pixels corresponding to the PM semi-manually segmented in the average image (manual selection followed by removal of pixels with intensities below 25% of the maximum pixel intensity in the selected region).

**Figure 1-figure supplement 2. Spectral filters for two-species SFSCS. (A,B)** Photon weights calculated in spectral decomposition of SFSCS data acquired on HEK 293T cells expressing mp-mEYFP-mEGFP (A) or mp-mCherry2-mApple (B).

**Figure 1-figure supplement 3. SFSCS on FP hetero-dimers. (A)** Representative CFs (green: ACF for mEGFP ("G"), yellow: ACF for mEYFP ("Y"), grey: CCF calculated between both fluorophore signals) obtained from SFSCS measurements on the PM of living HEK 293T cells expressing mp-mEYFP-mEGFP hetero-dimers. Solid thick lines show fits of a two-dimensional diffusion model to the CFs. **(B)** Representative CFs (light red: ACF for

mApple ("A"), dark red: ACF for mCherry2 ("Ch2), grey: CCF calculated between both fluorophore signals) obtained from SFSCS measurements on the PM of living HEK 293T cells expressing mp-mCherry2-mApple hetero-dimers. Solid thick lines show fits of a two-dimensional diffusion model to the CFs. **(C)** Relative cross-correlation values obtained from SFSCS measurements on HEK 293T cells expressing mp-mEYFP-mEGFP (rigid linker between the two FPs, see supplementary file 1a) or mp-mEGFP-mEYFP (short linker between the two FPs, supplementary file 1a) hetero-dimers. Data are pooled from three independent experiments each. The number of cells measured is given in parentheses. Error bars represent mean±SD. Statistical significance was determined using Welch's corrected two-tailed student's *t*-test (**$P<0.05$).

We furthermore verified that SFSCS analysis results in correct estimates of protein diffusion dynamics. To this aim, we co-expressed mEGFP-tagged IAV hemagglutinin spike transmembrane protein (HA-mEGFP) and mp-mEYFP. We then compared the diffusion times measured by SFSCS to the values obtained on cells expressing each of the two constructs separately (Fig.2A). For HA-mEGFP, an average diffusion time of 36±8 ms (mean±SD, n=18 cells) was determined in cells expressing both proteins. This value was comparable to that measured for HA-mEGFP expressed separately (34±9 ms, mean±SD, n=21 cells). For mp-mEYFP, diffusion times of 8±2 ms and 9±3 ms were measured in samples expressing both proteins or just mp-mEYFP, respectively. In addition to diffusion analysis, we also analyzed the cross-correlation of HA-mEGFP and mp-mEYFP signal for two-species measurements, resulting in negligible rel.cc. values close to zero (Figure 2-figure supplement 1). Hence, SFSCS yielded correct estimates of diffusion dynamics and allowed to distinguish faster and slower diffusing protein species tagged with spectrally strongly overlapping FPs.

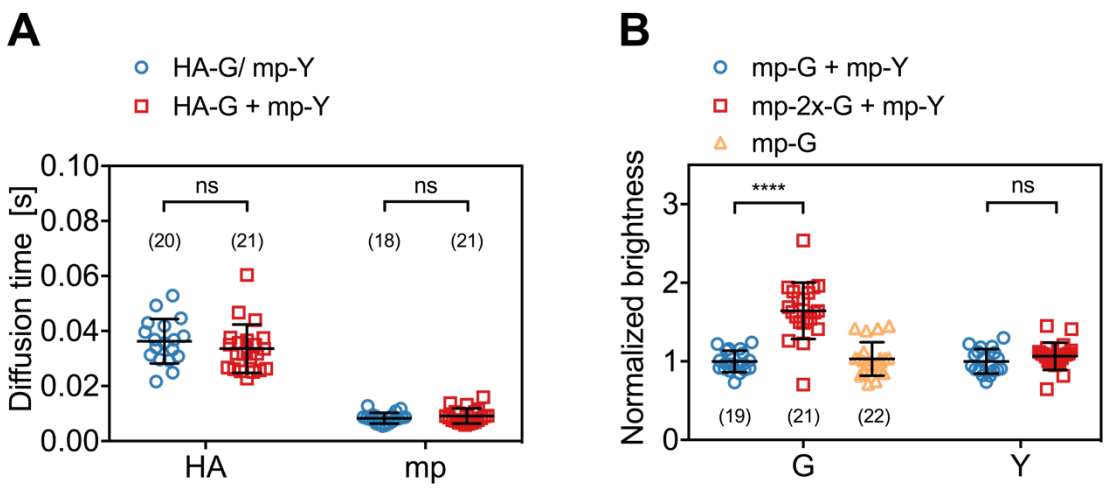

**Figure 2. Diffusion and molecular brightness analysis for two-species SFSCS measurements at the PM of HEK 293T cells. (A)** Diffusion times obtained from SFSCS measurements on HEK 293T cells expressing either IAV HA-mEGFP or mp-mEYFP separately (blue), or co-expressing both fusion proteins (red). **(B)** Normalized molecular brightness values obtained from SFSCS measurements on HEK 293T cells co-expressing mp-mEGFP and mp-mEYFP (blue), mp-2x-mEGFP and mp-mEYFP (red), or expressing mp-mEGFP alone (yellow). Normalized brightness values were calculated by dividing molecular brightness values detected in each SFSCS measurement by the average brightness obtained for mEGFP and mEYFP in cells co-expressing mp-mEGFP and mp-mEYFP. Data are pooled from two independent experiments for each sample. The number of cells measured is given in parentheses. Error bars represent mean±SD. Statistical significance was determined using Welch's corrected two-tailed student's *t*-test (****$P$<0.0001, ns: not significant).

**Figure 2-figure supplement 1. Relative cross-correlation obtained from described two-species SFSCS measurements.** The number of cells measured is given in parentheses. Error bars represent mean±SD.

Finally, we evaluated the capability of SFSCS to precisely determine the molecular brightness, as a measure of protein oligomerization. We compared the molecular brightness values for mEGFP and mEYFP in samples co-expressing monomeric FP constructs mp-mEGFP and mp-mEYFP with the values obtained for cells co-expressing mp-2x-mEGFP homo-dimers and mp-mEYFP (Fig.2B). From SFSCS analysis of measurements in the latter sample, we obtained a normalized molecular brightness of 1.64±0.36 (mean±SD, n=21 cells) for mEGFP, relative to the brightness determined in the monomer sample (n=19 cells). This value is in agreement with our previous quantification of the relative brightness of mEGFP homo-dimers, corresponding to a fluorescence probability ($p_f$) of ca. 60-75% for mEGFP (14). The $p_f$ is an empirical, FP-specific parameter that was previously characterized for multiple FPs (14). It quantifies the fraction of non-fluorescent FPs due to photophysical processes, such as transitions to long-lived dark states, or slow FP maturation and needs to be taken into account to correctly determine the oligomerization state of FP tagged protein complexes. As a reference for the absolute brightness, we also determined the relative molecular brightness of mEGFP in cells expressing mp-mEGFP alone, yielding a value of 1.03±0.21 (mean±SD, n=22 cells). Additionally, the brightness values determined for mEYFP in both two-species samples were similar, with a relative ratio of 1.07±0.18, as expected. This confirms that reliable brightness values were obtained and that dimeric and monomeric species can be correctly identified.

247 In summary, these results demonstrate that SFSCS analysis of fluorescence fluctuations
248 successfully separates the contributions of FPs exhibiting strongly overlapping emission
249 spectra, yielding correct quantitative estimates of protein oligomerization and diffusion
250 dynamics.
251
252 **Simultaneous cross-correlation and brightness analysis for three spectrally overlapping**
253 **FPs at the PM**
254 In the previous section, we showed that SFSCS enables cross-talk-free cross-correlation
255 analysis of two fluorescent species excited with a single laser line, even in the case of strongly
256 overlapping emission spectra. To explore the full potential of SFSCS, we extended the approach
257 to systems containing three spectrally overlapping fluorophores. We excited mEGFP, mEYFP,
258 and mCherry2 with 488 nm and 561 nm lines simultaneously and detected their fluorescence
259 in 23 spectral bins in the range of 491 nm to 695 nm. We measured individual emission spectra
260 (Figure 1-figure supplement 1) for single species samples to calculate three-species spectral
261 filters (Figure 3-figure supplement 1), which we then used to decompose the signal detected in
262 cells expressing multiple FPs into the contribution of each species.
263 As a first step, we performed three-species SFSCS measurements on HEK 293T cells co-
264 expressing mp-mEYFP with either i) mp-mEGFP and mp-mCherry2 (mp-G + mp-Y + mp-
265 Ch2) or ii) mp-mCherry2-mEGFP hetero-dimers (mp-Ch2-G + mp-Y). Additionally, we tested
266 a sample with cells expressing mp-mEYFP-mCherry2-mEGFP hetero-trimers (mp-Y-G-Ch2).
267 We then calculated ACFs for all three FP species and CCFs all fluorophore combinations,
268 respectively. In the first sample (mp-G + mp-Y + mp-Ch2), in which all three FPs are anchored
269 independently to the PM, we obtained CCFs fluctuating around zero for all fluorophore
270 combinations, as expected (Fig.3A). In the second sample (mp-Ch2-G + mp-Y), a substantial
271 cross-correlation was detected between mEGFP and mCherry2, whereas the other two
272 combinations resulted in CCFs fluctuating around zero (Fig.3B). In the hetero-trimer sample,

273 CCFs with low level of noise and amplitudes significantly above zero were successfully
274 obtained for all three fluorophore combinations (Fig.3C). From the amplitude ratios of the
275 ACFs and CCFs, we then calculated rel.cc. values for all measurements (Fig.3F). Low rel.cc.
276 values were obtained for all fluorophore combinations that were not expected to show
277 interactions, e.g. 0.05±0.08 (mean±SD, n=46 cells) between mEGFP and mEYFP signal in the
278 first sample. It is worth noting that these values, albeit consistently negligible, appear to depend
279 on the specific fitting procedure (see Figure 3-figure supplement 2 and Methods for details).
280 For mEGFP and mCherry2, similar rel.cc. values of 0.45±0.06 (mean±SD, n=20 cells) and
281 0.56±0.08 (mean±SD, n=17 cells) were observed in cells expressing mp-mCherry2-mEGFP
282 hetero-dimers or mp-mEYFP-mCherry2-mEGFP hetero-trimers. The minor difference could
283 be attributed e.g. to different linker peptides (i.e. long rigid linker between FPs in hetero-trimers
284 and a short flexible linker in hetero-dimers), increasing the degree of FRET between mEGFP
285 and mCherry2 in hetero-dimers and reducing the cross-correlation. The hetero-trimer sample
286 showed high rel.cc. values also for the other two fluorophore combinations: mEGFP and
287 mEYFP ($rel.cc._{G,Y}$=0.79±0.12) or mCherry2 and mEYFP ($rel.cc._{Y,Ch2}$=0.57±0.07).
288

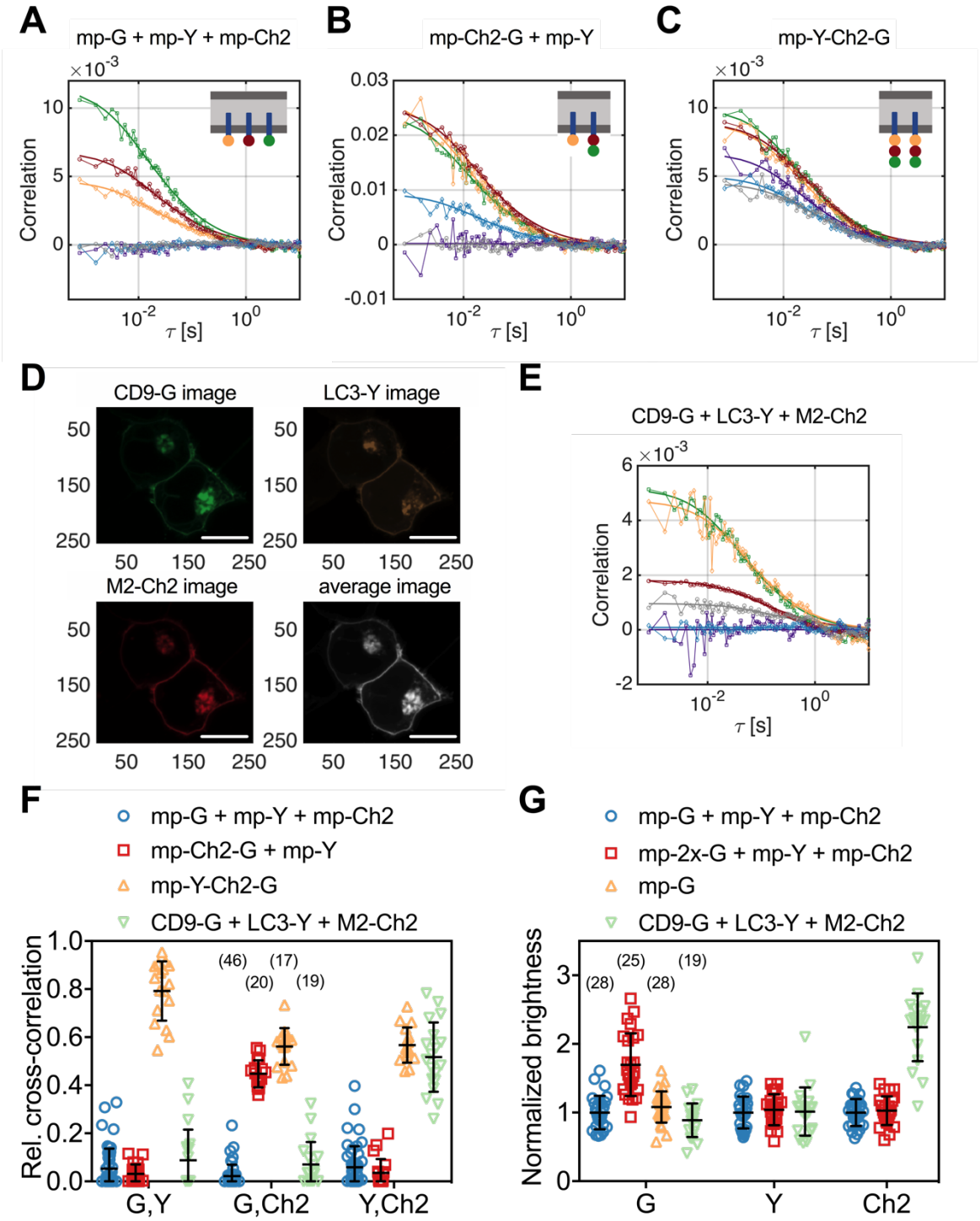


**Figure 3. Cross-correlation and molecular brightness analysis for three-species SFSCS measurements on FP hetero-oligomers and IAV M2 at the PM of HEK 293T cells. (A-C)** Representative CFs (green/yellow/red: ACFs for mEGFP ("G")/ mEYFP ("Y")/ mCherry2 ("Ch2"), purple/blue/grey: CCFs calculated for the pairs mEGFP and mEYFP/ mEGFP and mCherry2/ mEYFP and mCherry2) obtained from three-species SFSCS measurements on HEK 293T cells co-expressing mp-mEGFP, mp-mEYFP, and mCherry2 (A), mp-mCherry2-mEGFP hetero-dimers and mp-mEYFP (B), or expressing mp-mEYFP-mCherry2-mEGFP hetero-trimers (C), as illustrated in insets. Solid thick lines show fits of a two-dimensional diffusion model to the CFs. **(D)** Representative fluorescence images of HEK 293T cells co-expressing CD9-mEGFP, LC3-mEYFP, and IAV protein M2-mCh2. Spectral filtering and decomposition were performed to obtain a single image for each species. Scale bars are 5 µm. **(E)** Representative CFs (green/yellow/red: ACFs for mEGFP/mEYFP/mCherry2, purple/blue/grey: CCFs calculated for the pairs mEGFP and mEYFP/ mEGFP and mCherry2/ mEYFP and mCherry2) obtained from three-species SFSCS measurements on HEK 293T cells co-expressing CD9-mEGFP, LC3-mEYFP, and M2-mCh2. Solid thick lines show fits of a two-dimensional diffusion model to the CFs. **(F)** Relative cross-correlation values

obtained from three-species SFSCS measurements described in (A-C) and I. **(G)** Normalized molecular brightness values obtained from three-species SFSCS measurements on HEK 293T cells co-expressing mp-mEGFP, mp-mEYFP, and mp-mCherry2 (blue), mp-2x-mEGFP, mp-mEYFP, and mp-mCherry2 (red), CD9-mEGFP, LC3-mEYFP, and M2-mCh2 (green), or expressing mp-mEGFP alone (yellow). Normalized brightness values were calculated by dividing the molecular brightness values detected in each SFSCS measurement by the average brightness obtained for mEGFP, mEYFP, and mCherry2 in cells co-expressing mp-mEGFP, mp-mEYFP, and mp-mCherry2. Data are pooled from two independent experiments for each sample. The number of cells measured is given in parentheses. Error bars represent mean±SD.

**Figure 3-figure supplement 1. Spectral filters for three-species SFSCS.** Photon weights calculated in spectral decomposition of SFSCS data acquired on HEK 293T cells expressing mp-mEYFP-mCherry2-mEGFP. Shown are average photon weights from five SFSCS acquisitions each.

**Figure 3-figure supplement 2. Relative cross-correlation for described three-species SFSCS, analyzed using different fitting algorithms.** CCFs obtained from measurements on cells co-expressing mp-mCherry2-mEGFP hetero-dimers and mp-mEYFP were fitted using as start parameter for the amplitude either a positive value (same for all CCFs, fit routine 1), or the average of the first five points of each CCF (fit routine 2). For non-correlated data (e.g. G,Y and Y,Ch2 combinations), the second fit routine may converge to negative fit amplitudes, resulting in a distribution of rel.cc. values scattered around 0. Fit routine 1 always converged to positive amplitude values, producing low but positive rel.cc. values. Filtering based on the cross-correlation diffusion time (fit routine 1, filtered) removes some of the residual positive rel.cc. in non-correlated data. Here a threshold value of five times the maximum of the two diffusion times obtained from ACFs for each respective FP combination was chosen. For correlated data, e.g. G,Ch2, both fit routines converged to comparable positive values.

**Figure 3-figure supplement 3. Noise analysis of described three-species SFSCS measurements.** SNR (color coded) of ACFs for mEGFP (A), mEYFP (B), and mCherry2 (C) channels obtained from SFSCS measurements on HEK 293T cells co-expressing mp-mEGFP, mp-mEYFP, and mp-mCherry2, as a function of their signal relative to that of the other two FP species. Data was pooled from two independent experiments in which 31 cells were measured in total.

**Figure 3-figure supplement 4. Membrane recruitment of LC3 in M2 expressing cells. (A,B)** Fluorescence images of LC3-mEYFP (A) and M2-mCherry2 (B) excited with either 488 nm (A) or 561 nm (B) excitation. LC3 is recruited to the PM in cells showing higher expression of M2 (top cell) relative to M2, but remains in the cytosol in cells expressing only low levels of M2 compared to LC3 (bottom cell). Scale bars are 10 µm. **(C)** Molecular brightness of LC3-mEYFP obtained from three-species SFSCS measurements shown in Fig.3, as a function of the ratio of LC3-mEYFP to M2-mCherry2 expression at the PM, in units of protein monomers. The number of monomers was calculated by dividing the signal detected for LC3-mEYFP/M2-mCherry2 in SFSCS measurements by the average molecular brightness detected for mEYFP and mCherry2 fluorophores in the monomeric reference sample (cells co-expressing mp-mEGFP, mp-mEYFP, and mp-mCherry2, Fig.3).

In addition to cross-correlation analysis, we performed molecular brightness measurements on samples containing three FP species. In particular, we compared molecular brightness values obtained by SFSCS on HEK 293T cells co-expressing homo-dimeric mp-2x-mEGFP, mp-mEYFP, and mp-mCherry2 (mp-2x-G + mp-Y + mp-Ch2) to the values measured on cells co-expressing the three monomeric constructs mp-mEGFP, mp-mEYFP, and mp-mCherry2 (mp-G + mp-Y + mp-Ch2). Whereas similar brightness values were obtained for mEYFP and mCherry2 in both samples, e.g. relative brightness of 1.04±0.23 for mEYFP and 1.03±0.21 for mCherry2 (mean±SD, n=25 cells/ n=28 cells), a higher brightness of 1.70±0.46 was measured

352 for mEGFP in the first sample (Fig.3G). This value corresponds to a $p_f$ of ca. 70% for mEGFP,
353 as expected (14). To confirm that absolute brightness values are not influenced by the spectral
354 decomposition, we also determined the brightness of mEGFP in cells expressing mp-mEGFP
355 alone (Fig.3G), resulting in values close to 1 (1.08±0.23, mean±SD, n=28 cells).
356

357 **The IAV protein M2 interacts strongly with LC3 but not with CD9**

358 Having demonstrated the capability of SFSCS to successfully quantify protein interactions and
359 oligomerization, even in the case of three FPs with overlapping emission spectra, we applied
360 this approach in a biologically relevant context. In more detail, we investigated the interaction
361 of IAV channel protein M2 with the cellular host factors CD9 and LC3. CD9 belongs to the
362 family of tetraspanins and is supposedly involved in virus entry and virion assembly (31–33).
363 The autophagy marker protein LC3 was recently shown to be recruited to the PM in IAV-
364 infected cells (see also Figure 3-figure supplement 4A,B), promoting filamentous budding and
365 virion stability, thus indicating a role of LC3 in virus assembly (34). To detect hetero-
366 interactions between CD9, LC3 and M2, we co-expressed the fluorescent fusion proteins CD9-
367 mEGFP, LC3-mEYFP and M2-mCherry2 (i.e. M2 carrying an mCherry2 tag at the extracellular
368 terminus) in HEK 293T cells (Fig.3D) and performed three-species SFSCS measurements at
369 the PM (Fig.3E).

370 We then calculated rel.cc. values to quantify pair-wise interactions of the three proteins
371 (Fig.3F). The obtained rel.cc. values for CD9-mEGFP with LC3-mEYFP or M2-mCherry2
372 ($rel.cc._{CD9\text{-}G,LC3\text{-}Y}$=0.09±0.13,$rel.cc._{CD9\text{-}G,M2\text{-}Ch2}$=0.07±0.09, mean±SD, n=19 cells) were similar
373 to those of the negative cross-correlation control (i.e. cells co-expressing mp-mEGFP, mp-
374 mEYFP and mp-mCherry2, see previous paragraph). In contrast, we detected a substantial
375 rel.cc. of 0.52±0.14 for LC3-mEYFP and M2-mCherry2. This value was close (ca. 90% on
376 average) to that obtained for this fluorophore combination in measurements on FP hetero-
377 trimers, suggesting very strong association of LC3-mEYFP with M2-mCherry2. We

378 furthermore analyzed the molecular brightness for each species, normalized to the monomeric
379 references (Fig.3G). While CD9-mEGFP and LC3-mEYFP showed normalized brightness
380 values close to 1 ($B_{CD9\text{-}G}$=0.89±0.25, $B_{LC3\text{-}Y}$=1.02±0.35), suggesting that both proteins are
381 monomers, we observed significantly higher relative brightness values for M2-mCherry2 ($B_{M2\text{-}}$
382 $_{Ch2}$=2.24±0.49). Assuming a $p_f$ of ca. 60% for mCherry2 (14), the determined relative brightness
383 corresponds to an oligomerization state of $\varepsilon_{M2-Ch2} = 3.1 \pm 0.8$, i.e. formation of M2 dimers to
384 tetramers at the PM.
385
386 **SFSCS allows simultaneous analysis of protein-protein interactions for four spectrally**
387 **overlapping FP species**
388 Having demonstrated robust three-species cross-correlation analysis, we aimed to further
389 explore the limits of SFSCS. We investigated therefore whether SFSCS can discriminate of
390 differential interactions between four species using the spectral emission patterns of mEGFP,
391 mEYFP, mApple and mCherry2 for spectral decomposition (Figure 1-figure supplement 1,
392 Figure 4-figure supplement 1). As a proof of concept, we performed four-species measurements
393 on three different samples: i) cells co-expressing all four FPs independently as membrane-
394 anchored proteins (mp-G + mp-Y + mp-A + mp-Ch2), ii) cells co-expressing mp-mCherry2-
395 mEGFP hetero-dimers, mp-mEYFP, and mp-mApple (mp-Ch2-G + mp-Y + mp-A), iii) cells
396 expressing mp-mEYFP-mCherry2-mEGFP-mApple hetero-tetramers (mp-Y-Ch2-G-A). We
397 then calculated four ACFs, six CCFs, and rel.cc. values from the amplitude ratios of the ACFs
398 and CCFs. For all fluorophore species, ACFs with amplitudes significantly above zero were
399 obtained. ACFs calculated for mEGFP and mEYFP were characterized by a higher SNR
400 compared to those for the red FPs mApple and, in particular, mCherry2 (Fig.4A-C).
401 Nevertheless, reasonable diffusion time values could be determined for all species, showing the
402 largest variation for mCherry2 (Figure 4-figure supplement 2).

403 Noise levels of the CCFs were moderate (Fig.4D-F), yet allowing robust fitting and estimation
404 of cross-correlation amplitudes. Based on the determined rel.cc. values (Fig.4G), the different
405 samples could successfully be discriminated. In the first sample (mp-G + mp-Y + mp-A + mp-
406 Ch2), neglibile to very low values were obtained, i.e. at maximum 0.11±0.11 (mean±SD, n=12
407 cells) for mApple and mCherry2. In the second sample (mp-Ch2-G + mp-Y + mp-A), similarly
408 low rel.cc. values were obtained for all fluorophore combinations, e.g. 0.10±0.10 (mean±SD,
409 n=13 cells) for mApple and mCherry2, with the exception of mEGFP and mCherry2, showing
410 an average value of 0.55±0.13. For the hetero-tetramer sample, high rel.cc. values were
411 measured for all fluorophore combinations, ranging from 0.42±0.07 (mean±SD, n=15 cells) for
412 mEGFP and mApple to 0.78±0.08 for mEGFP and mEYFP. Notably, a significant rel.cc. of
413 0.53±0.10 was also determined for mApple and mCherry2 signals, i.e. from the CCFs
414 exhibiting the lowest SNR.
415
416

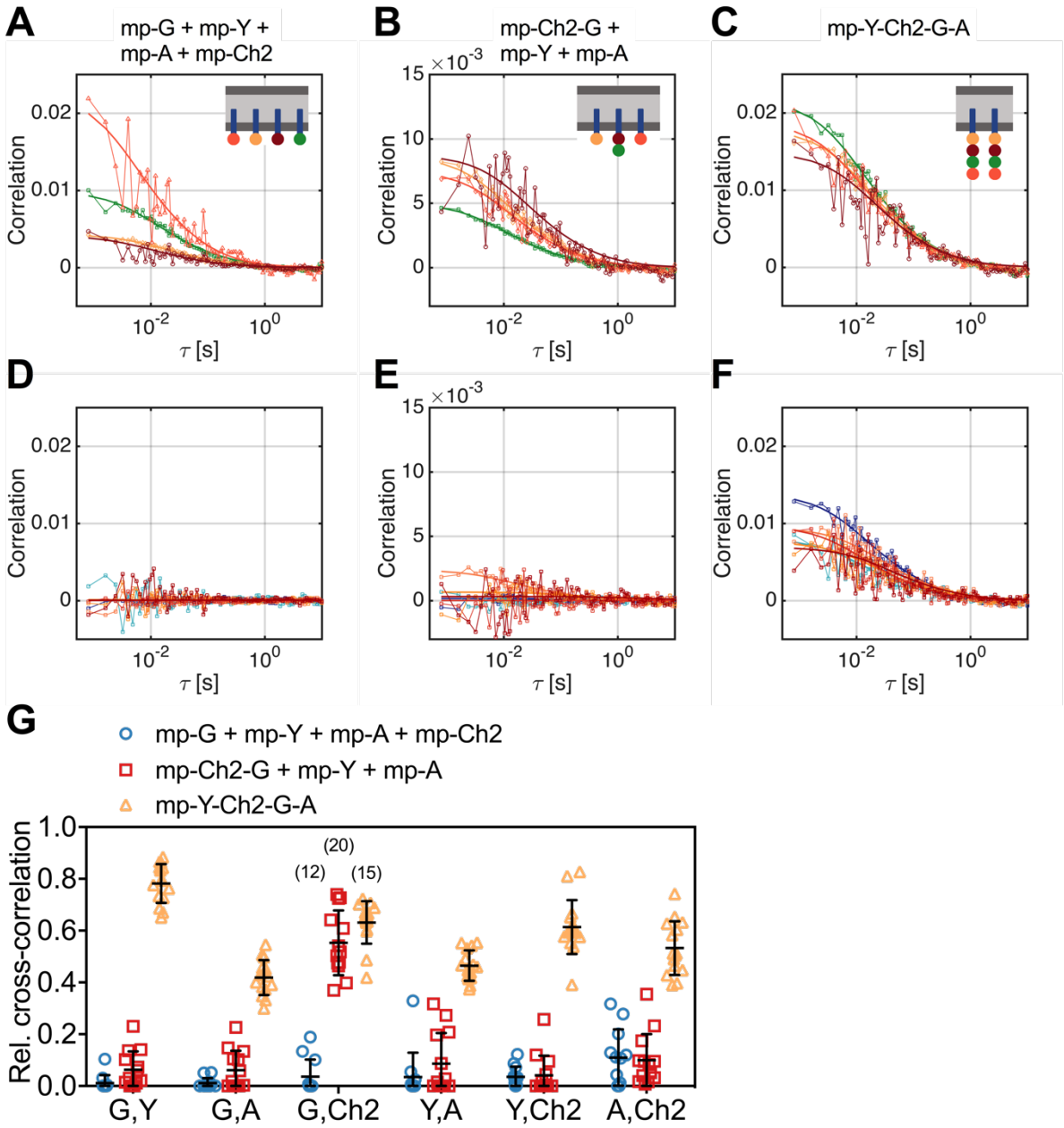


**Figure 4. Cross-correlation analysis for four-species SFSCS measurements on FP hetero-oligomers in HEK 293T cells. (A-C)** Representative ACFs (green/yellow/orange/red for mEGFP ("G")/ mEYFP ("Y")/ mApple ("A")/ mCherry2 ("Ch2")) obtained from four-species SFSCS measurements on HEK 293T cells co-expressing mp-mEGFP, mp-mEYFP, mp-mApple, and mCherry2 (A), mp-mCherry2-mEGFP hetero-dimers, mp-mEYFP, and mp-mApple (B), or expressing mp-mEYFP-mCherry2-mEGFP-mApple hetero-tetramers (C), as illustrated in insets. Solid thick lines show fits of a two-dimensional diffusion model to the CFs. **(D-F)** SFSCS CCFs (dark blue/ light blue/ orange/ yellow/ red/ dark red for CCFs calculated for mEGFP and mEYFP/ mEGFP and mApple/ mEGFP and mCherry2/ mEYFP and mApple/ mEYFP and mCherry2/ mApple and mCherry2) from measurements described in (A-C) (CCFs in (I(E)/(F) corresponding to ACFs shown in (A)/(B)/(C)). Solid thick lines show fits of a two-dimensional diffusion model to the CFs. **(G)** Relative cross-correlation values obtained from four-species SFSCS measurements described in (A-C). Data are pooled from two independent experiments. The number of cells measured is given in parentheses. Error bars represent mean±SD.

**Figure 4-figure supplement 1. Spectral filters for four-species SFSCS.** Photon weights calculated in spectral decomposition of SFSCS data acquired on HEK 293T cells expressing mp-mEYFP-mCherry2-mEGFP-mApple. Shown are average photon weights from five SFSCS acquisitions each.

**Figure 4-figure supplement 2. Diffusion dynamics of four-species SFSCS measurements.** Diffusion times obtained from four-species SFSCS measurements on HEK 293T cells co-expressing mp-mEGFP, mp-mEYFP,

437 mp-mApple, and mCherry2 (blue), mp-mCherry2-mEGFP hetero-dimers, mp-mEYFP, and mp-mApple (red), or
438 expressing mp-mEYFP-mCherry2-mEGFP-mApple hetero-tetramers (yellow). The four FP species are denoted
439 with "G", "Y", "A", "Ch2". Data are pooled from two independent experiments. The number of cells measured is
440 given in parentheses. Error bars represent mean±SD.
441
442
443 **RSICS can be extended to simultaneous detection of four fluorophore species**

444 Having identified a set of FPs that is compatible with four-species SFSCS, we aimed to extend
445 the recently presented RSICS method (27) to applications with four fluorophore species being
446 detected simultaneously. To test the effectiveness of this approach, we carried out
447 measurements in the cytoplasm of living A549 cells co-expressing mEGFP, mEYFP, mApple,
448 and mCherry2 in several configurations, similar to the SFSCS experiments presented in the
449 previous paragraph. In more detail, we performed four-species RSICS measurements on the
450 following three samples: i) cells co-expressing free mEGFP, mEYFP, mApple, and mCherry2
451 (1x-G + 1x-Y + 1x-A + 1x-Ch2), ii) cells co-expressing mCherry2-mEGFP and mEYFP-
452 mApple hetero-dimers (Ch2-G + Y-A), iii) cells expressing mEYFP-mCherry2-mEGFP-
453 mApple hetero-tetramers (Y-Ch2-G-A). Representative CFs obtained following RSICS
454 analysis with arbitrary region selection (35) are shown in Fig.5. In all samples, ACFs with
455 amplitudes significantly above zero were obtained, with the highest noise level detected for
456 mCherry2 (Fig.5A,C,E). A three-dimensional diffusion model could be successfully fitted to
457 all detected ACFs.
458 Detected CCFs showed the expected pattern: all six CCFs were indistinguishable from noise
459 for the first sample with four independent FPs (Fig.5B), whereas large CCF amplitudes were
460 obtained for the pairs mEGFP and mCherry2, as well as mEYFP and mApple in the second
461 sample (Ch2-G + Y-A) (Fig.5D). Also, significantly large amplitudes were observed for all six
462 CCFs for the hetero-tetramer sample, albeit with different levels of noise. For example, the
463 lowest SNR was observed in CCFs for mApple and mCherry2 (Fig.5F).
464

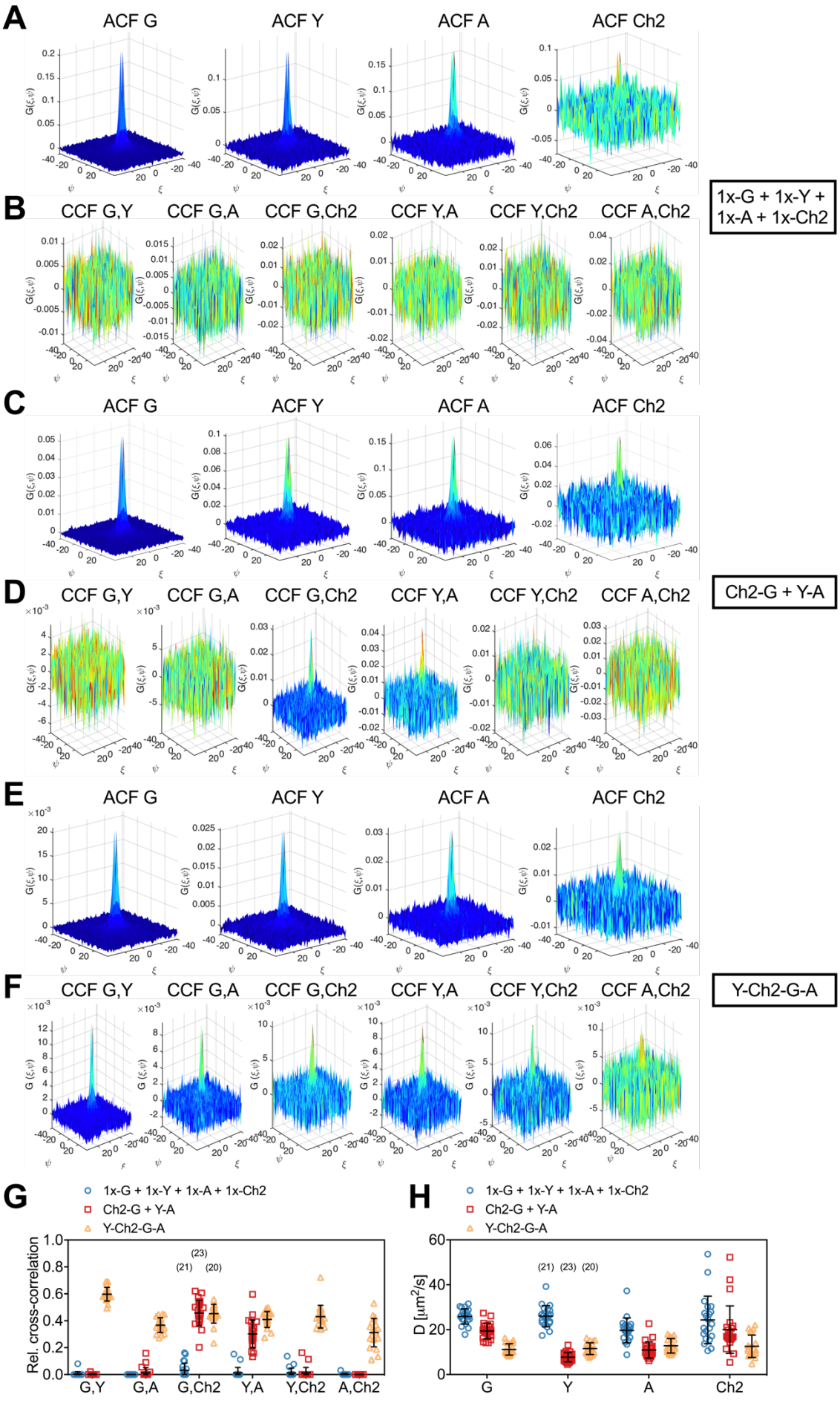
A
ACF G
ACF Y
ACF A
ACF Ch2
B
CCF G,Y
CCF G,A
CCF G,Ch2
CCF Y,A
CCF Y,Ch2
CCF A,Ch2
1x-G + 1x-Y + 1x-A + 1x-Ch2
C
ACF G
ACF Y
ACF A
ACF Ch2
D
CCF G,Y
CCF G,A
CCF G,Ch2
CCF Y,A
CCF Y,Ch2
CCF A,Ch2
Ch2-G + Y-A
E
ACF G
ACF Y
ACF A
ACF Ch2
F
CCF G,Y
CCF G,A
CCF G,Ch2
CCF Y,A
CCF Y,Ch2
CCF A,Ch2
Y-Ch2-G-A
G
1x-G + 1x-Y + 1x-A + 1x-Ch2
Ch2-G + Y-A
Y-Ch2-G-A
Rel. cross-correlation
(23)
(21) (20)
G,Y
G,A
G,Ch2
Y,A
Y,Ch2
A,Ch2
H
1x-G + 1x-Y + 1x-A + 1x-Ch2
Ch2-G + Y-A
Y-Ch2-G-A
D [μm²/s]
(21) (23) (20)
G
Y
A
Ch2

466 **Figure 5. Cross-correlation analysis for four-species RSICS measurements on FP hetero-oligomers**
467 **expressed in cytoplasm of A549 cells. (A-F)** Representative RSICS spatial ACFs (A,C,E) and CCFs (B,D,F)
468 obtained from four-species RSICS measurements on A549 cells. Cells were co-expressing mEGFP ("G"), mEYFP
469 ("Y"), mApple ("A"), mCherry2 ("Ch2") (A,B), mCherry2-mEGFP and mEYFP-mApple heterodimers (C,D), or
470 mEYFP-mCherry2-mEGFP-mApple hetero-tetramers (E,F). **(G,H)** Relative cross-correlation values (G) and
471 diffusion coefficients (H) obtained from four-species RSICS measurements described in (A-F). Data are pooled
472 from two independent experiments. The number of cells measured is given in parentheses. Error bars represent
473 mean±SD.
474
475 **Figure 5-figure supplement 1. FP emission spectra.** Average emission spectra measured on HEK 293T cell
476 samples (solid line) described in Figure 1-figure supplement 1, or on A549 cells expressing cytosolic mEGFP,
477 mEYFP, mApple, mCherry2 (dotted line). Spectra measured on four cells each were averaged over three (HEK
478 293T) or two (A549) days. For A549 cells, a homogeneous ROI in the cytosol was manually selected.
479
480 **Figure 5-figure supplement 2. FP emission spectra at different pH values. (A-D)** Average emission spectra of
481 GPI-mEGFP (A), GPI-mEYFP (B), GPI-mApple (C), and GPI-mCherry2 (D) measured by spectral imaging (23
482 spectral channels from 491 nm to 695 nm) using 488 nm and 561 nm excitation on HEK 293T cells supplemented
483 with buffer at different pH values, ranging from pH 5.0 to pH 9.2. At each pH value, ca. 10-20 cells were imaged
484 for five frames. To obtain average emission spectra, pixels corresponding to the PM were semi-manually
485 segmented (manual selection followed by removal of pixels with intensities below 25% of the maximum pixel
486 intensity in the selected region) and detected spectra averaged over all pixels and cells measured at each pH.
487
488

489 From the amplitude ratios of ACFs and CCFs, we determined rel.cc. values (Fig.5G). This
490 analysis resulted in negligible values for the first sample (1x-G + 1x-Y + 1x-A + 1x-Ch2), e.g.
491 $rel.cc._{G,Ch2}$=0.03±0.05 (mean±SD, n=21 cells). For the second sample (Ch2-G + Y-A), values
492 significantly above zero, i.e. $rel.cc._{G,Ch2}$=0.46±0.09 (mean±SD, n=23 cells) and
493 $rel.cc._{Y,A}$=0.30±0.10, were only observed for two fluorophore pairs. For the third sample, cells
494 expressing mEYFP-mCherry2-mEGFP-mApple hetero-tetramers (Y-Ch2-G-A), rel.cc. values
495 significantly above zero were obtained for all FP pairs, ranging from $rel.cc._{A,Ch2}$=0.31±0.11
496 (mean±SD, n=20 cells) to $rel.cc._{G,Y}$=0.60±0.05. Notably, rel.cc. values obtained for the FP
497 species correlating in the second sample (Ch2-G + Y-A) were similar in the third sample (Y-
498 Ch2-G-A), e.g. $rel.cc._{G,Ch2}$=0.45±0.07 and $rel.cc._{Y,A}$=0.41±0.06. The lower rel.cc. value
499 measured for mEYFP and mApple in hetero-dimers (Ch2-G + Y-A) could be attributed to
500 different linker sequences (long rigid linker in hetero-dimers vs. mCherry2-mEGFP and three
501 long rigid linkers as spacer in hetero-tetramers (Y-Ch2-G-A)), possibly affecting FRET
502 between neighboring FPs.

503 Finally, we analyzed the diffusion dynamics of FP fusion proteins as determined from the
504 spatial dependence of the ACFs for the four fluorophore species. Diffusion coefficients (D)
505 obtained for mCherry2 showed the highest variation (Fig.5H), reflecting the reduced SNR for
506 this fluorophore. Nevertheless, similar average D values were determined for different
507 fluorophore species coupled as hetero-oligomers, e.g. $D_G$=19.4±3.4 $\mu m^2/s$ and $D_{Ch2}$=20±11
508 $\mu m^2/s$ (mean±SD, n=23 cells) for mEGFP-mCherry2 hetero-dimers, and $D_G$=11.2±2.5 $\mu m^2/s$,
509 $D_Y$=11.6±2.6 $\mu m^2/s$, $D_A$=12.8±3.2 $\mu m^2/s$, $D_{Ch2}$=12.6±5.0 $\mu m^2/s$ (mean±SD, n=20 cells) for
510 hetero-tetramers.

511 **Cross-correlation and molecular brightness analysis via three-species RSICS provide**
512 **stoichiometry of IAV polymerase complex assembly**

513 To test the versatility of three-species RSICS, we quantified intracellular protein interactions
514 and stoichiometries in a biologically relevant context. As an example, we focused on the
515 assembly of the IAV polymerase complex (PC), consisting of the three subunits polymerase
516 acidic protein (PA), polymerase basic protein 1 (PB1), and 2 (PB2). A previous investigation
517 using FCCS suggested an assembly model in which PA and PB1 form hetero-dimers in the
518 cytoplasm of cells. These are imported into the nucleus and appear to interact with PB2 to form
519 hetero-trimeric complexes (36). Nevertheless, this analysis could only be performed between
520 two of the three subunits at the same time. Also, the stoichiometry of the complex was reported
521 only for one of the three subunits, i.e. PA protein dimerization. Here, we labeled all three
522 subunits using FP fusion constructs and co-expressed PA-mEYFP, PB1-mEGFP, and PB2-
523 mCherry2 in A549 cells. We then performed three-species RSICS measurements in the cell
524 nucleus, where all three proteins are enriched (Fig.6A). RSICS analysis was performed on an
525 arbitrarily-shaped homogeneous region of interest in the nucleus. We then calculated RSICS
526 ACFs (Fig.6B), CCFs (Fig.6C), and rel.cc. values (Fig.6D) for the three fluorophore
527 combinations. The determined rel.cc. values were compared to the values obtained on negative

controls (i.e. cells co-expressing free mEGFP, mEYFP, and mCherry) and positive controls (i.e. cells expressing mEYFP-mCherry2-mEGFP hetero-trimers) (Fig.6D).

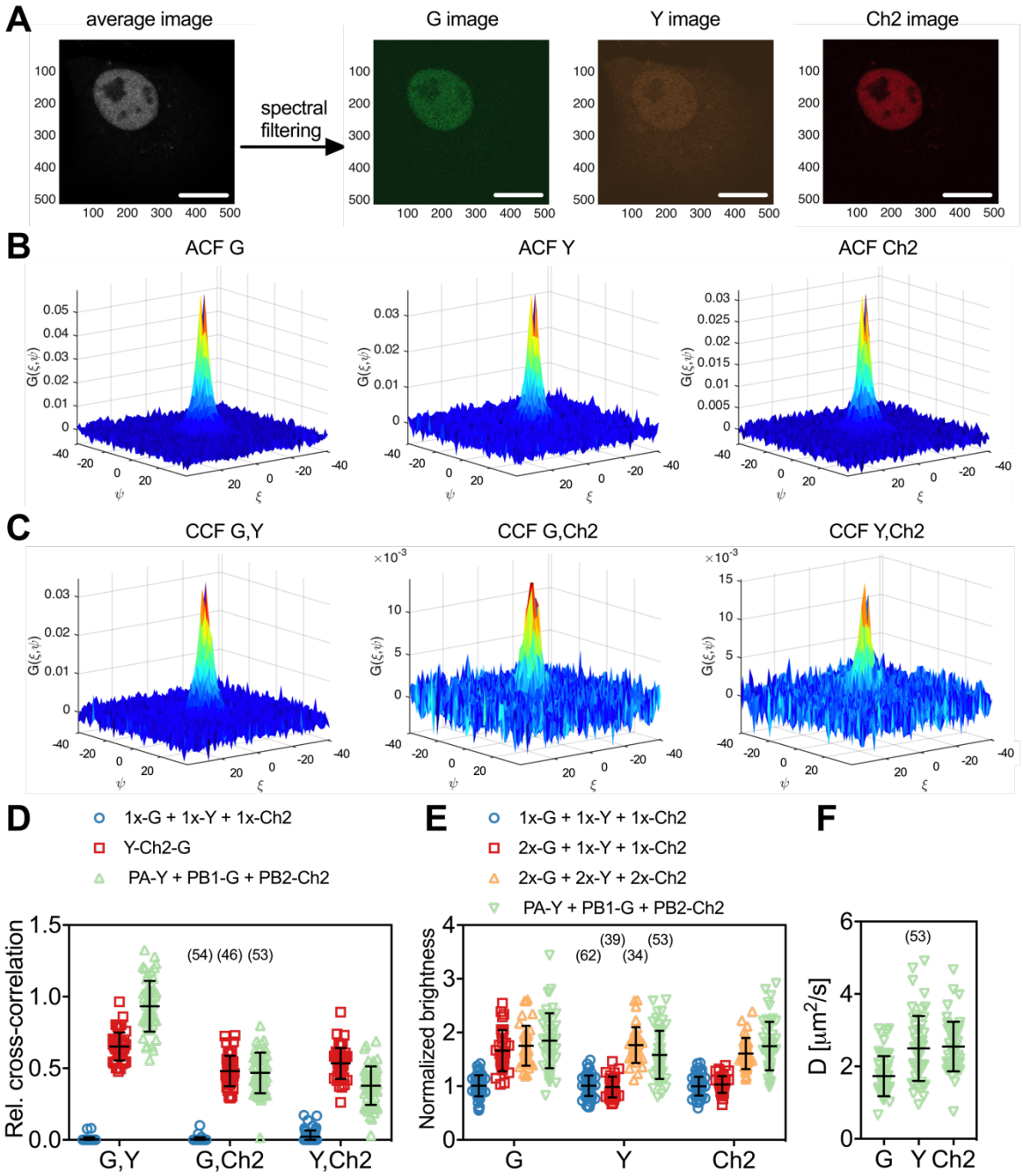


**Figure 6. Three-species RSICS measurements on IAV polymerase complex and FP hetero-oligomers in the nucleus of A549 cells. (A)** Representative fluorescence image (left) of A549 cells co-expressing FP-tagged IAV PC proteins PA-mEYFP, PB1-mEGFP, and PB2-mCherry2. Spectral filtering and decomposition result in a single image for each species (right), denoted with "Y", "G", and "Ch2". Scale bars are 10 µm. **(B,C)** Representative RSICS spatial ACFs (B) and CCFs (C) obtained from three-species RSICS measurements on A549 cells co-expressing PA-mEYFP, PB1-mEGFP, and PB2-mCherry2. **(D)** Relative cross-correlation values obtained from three-species RSICS measurements on A549 cells co-expressing mEGFP, mEYFP, and mCherry2 (blue), PA-mEYFP, PB1-mEGFP, PB2-mCherry2 (green), or expressing mEYFP-mCherry2-mEGFP hetero-trimers (red). Data are pooled from four independent experiments. **(E)** Normalized molecular brightness values obtained from three-species RSICS measurements on A549 cells co-expressing mEGFP, mEYFP, and mCherry2 (blue), 2x-mEGFP, mEYFP, and mCherry2 (red), 2x-mEGFP, 2x-mEYFP, 2x-mCherry2 (yellow), or PA-mEYFP, PB1-mEGFP, and PB2-mCherry2 (green). Data are pooled from three (2x-mEGFP + mEYFP + mCherry2, 2x-mEGFP

543 + 2x-mEYFP + 2x-mCherry2), four (PA-mEYFP + PB1-mEGFP + PB2-mCherry2), or five (mEGFP + mEYFP
544 + mCherry2) independent experiments. **(F)** Diffusion coefficients obtained from three-species RSICS
545 measurements on A549 cells co-expressing PA-mEYFP, PB1-mEGFP, and PB2-mCherry2. Data are pooled from
546 four independent experiments. For (D)-(F), the number of cells measured is given in parentheses. Error bars
547 represent mean±SD.
548
549 **Figure 6-figure supplement 1. Cross-correlation and diffusion analysis for three-species RSICS**
550 **measurements on IAV polymerase complex as a function of relative protein concentration. (A-C)** Relative
551 cross-correlation for PA-mEYFP and PB2-mCherry2 (A), normalized molecular brightness (B) and diffusion
552 coefficient (C) detected for PA-mEYFP, obtained from three-species RSICS measurements on A549 cells co-
553 expressing PA-mEYFP, PB1-mEGFP, and PB2-mCherry2. Data are plotted as a function of the ratio of PB1-
554 mEGFP to PA-mEYFP, in units of protein monomers, and pooled from four independent experiments (n=53 cells).
555 The number of monomers was calculated by dividing the signal detected for PB1-mEGFP and PA-mEYFP in
556 SFSCS measurements by the average molecular brightness detected for mEGFP and mEYFP fluorophores in the
557 monomeric reference sample (cells co-expressing mp-mEGFP, mp-mEYFP, and mp-mCherry2)
558
559
560 For the polymerase sample, high rel.cc. values were observed for all combinations: $rel.cc._{PB1-G,PA-Y}$=0.93±0.18
561 (mean±SD, n=53 cells), $rel.cc._{PB1-G,PB2-Ch2}$=0.47±0.14, $rel.cc._{PA-Y,PB2-Ch2}$=0.39±0.14. For the positive control, similar values were observed for mEGFP and
563 mCherry2, $rel.cc._{G,Ch2}$=0.48±0.11 (mean±SD, n=46 cells), whereas the values were higher than
564 that measured for PCs for mEYFP and mCherry2, $rel.cc._{Y,Ch2}$=0.53±0.11, and lower for mEGFP
565 and mEYFP, $rel.cc._{G,Y}$=0.65±0.10. The lower average rel.cc. between PA-mEYFP and PB2-
566 mCherry2 compared to the positive control indicates the presence of a minor fraction of non-
567 interacting PA and PB2. These proteins could be present in the nucleus in unbound form when
568 expressed in higher amount than PB1, since both PA and PB2 localize in the nucleus
569 individually and were previously shown not to interact when both present without PB1 (36).
570 This explanation is supported by the correlation between $rel.cc._{PA-Y,PB2-Ch2}$ and the relative
571 abundance of PB1-mEGFP (Figure 6-figure supplement 1A). Also, the observation that PB1 is
572 only transported to the nucleus in complex with PA is confirmed by the lower concentration of
573 PB1-mEGFP compared to PA-mEYFP in the nuclei of all measured cells (Figure 6-figure
574 supplement 1A). Thus, the fraction of PB1-mEGFP bound to PA-mEYFP should be as high as
575 the positive control, for a 1:1 stoichiometry. The observation of higher rel.cc. between mEGFP
576 and mEYFP for the polymerase subunits indicates higher order interactions, i.e. higher
577 stoichiometry than 1:1 (37).

578 To quantify the stoichiometry of the PC directly, we analyzed the molecular brightness of
579 RSICS measurements for all three fluorophore species. We normalized the obtained values to
580 the average values determined by RSICS on cells co-expressing monomeric mEGFP, mEYFP,
581 and mCherry2, measured on the same day. To test whether RSICS can be used to obtain reliable
582 brightness/oligomerization values for all fluorophore species, we first performed control
583 experiments on cells co-expressing either i) 2x-mEGFP homo-dimers with mEYFP and
584 mCherry monomers (2x-G + 1x-Y + 1x-Ch2) or ii) the three homo-dimers 2x-mEGFP, 2x-
585 mEYFP, and 2x-mCherry2 (2x-G + 2x-Y + 2x-Ch2). In the first sample, we observed an
586 increased relative brightness of 1.67±0.38 (mean±SD, n=34 cells) for mEGFP, whereas values
587 around 1 were obtained for mEYFP and mCherry2. This confirmed the presence of mEGFP
588 dimers as well as mEYFP and mCherry2 monomers in this control sample, as expected
589 (Fig.6E). In the sample containing all three homo-dimers, increased relative brightness values
590 were observed for all fluorophore species: 1.75±0.37 (mean±SD, n=39 cells) for mEGFP,
591 1.77±0.33 for mEYFP, and 1.61±0.29 for mCherry2 (see supplementary file 1b for data on day-
592 to-day variations). These values indicate successful determination of the dimeric state of all
593 three FP homo-dimers and are in good agreement with previous brightness measurements on
594 homo-dimers of mEGFP, mEYFP and mCherry2, corresponding to $p_f$ values of 60-75% (14).
595 Next, we proceeded with the analysis of PC oligomerization. For each polymerase subunit,
596 relative brightness values close to the values of homo-dimers were observed. Assuming $p_f$
597 values of 75%, 77%, and 61% (as calculated from the determined relative brightness values of
598 homo-dimers) for mEGFP, mEYFP, and mCherry2, respectively, $p_f$ corrected normalized
599 brightness values of $\varepsilon_{PB1-G} = 2.1 \pm 0.7$ (mean±SD, n=53 cells), $\varepsilon_{PA-Y} = 1.8 \pm 0.6$, and
600 $\varepsilon_{PB2-Ch2} = 2.2 \pm 0.7$ were obtained (see methods for details). These results suggest a 2:2:2
601 stoichiometry of the IAV PC subunits. Finally, we analyzed the diffusion dynamics of PCs via
602 RSICS (Fig.6F). The average D measured for PB1-mEGFP, $D_{PB1-G}$=1.7±0.6 $\mu m^2/s$ (mean±SD,
603 n=53 cells), was ca. 30% lower than the diffusion coefficients determined for PA-mEYFP- and

604 PB2-mCherry2 ($D_{PA-Y}$=2.5±0.9 μm$^2$/s and $D_{PB2-Ch2}$=2.6±0.7 μm$^2$/s). This observation is
605 compatible with the above-mentioned presence of a minor fraction of unbound (and thus faster
606 diffusing) PA and PB2 (likely in cells with a lower amount of PB1). A more detailed analysis
607 of the data confirmed this interpretation: The molecular brightness and diffusion coefficient of
608 PA-mEYFP depended on the relative concentration of PB1-mEGFP and PA-mEYFP, i.e. lower
609 brightness and higher diffusion coefficients were obtained in cells where PA-mEYFP was
610 present at much higher concentrations than PB1-mEGFP (Figure 6-figure supplement 1B,C).
611

612 **Triple raster image correlation spectroscopy (TRICS) analysis provides direct evidence**
613 **for assembly of ternary IAV polymerase complexes**

614 To directly confirm that IAV PC subunits form ternary complexes in the cell nucleus, we
615 implemented a triple-correlation analysis (i.e. TRICS) to detect coincident fluctuations of the
616 signal emitted by mEGFP-, mEYFP- and mCherry2-tagged proteins. A similar analysis has
617 previously been presented for three-channel FCS measurements (e.g. fluorescence triple
618 correlation spectroscopy (21), triple-color coincidence analysis (20)), but was so far limited to
619 *in vitro* systems such as purified proteins (21) or DNA oligonucleotides (20) labeled with
620 organic dyes. We performed TRICS on data obtained on cells co-expressing PC subunits PA-
621 mEYFP, PB1-mEGFP, and PB2-mCherry2 or cells co-expressing free mEGFP, mEYFP, and
622 mCherry, as a negative triple-correlation control. To evaluate ternary complex formation, we
623 quantified the relative triple-correlation (rel.3C., see Materials and Methods) for both samples
624 from the amplitudes of the ACFs and triple-correlation functions (3CFs). Fig.7A and B show
625 representative 3CFs for the negative control and the PC sample, respectively. For the negative
626 control, we obtained rel.3C. values fluctuating around zero (Fig.7C), rel.3C.=-0.02±0.54
627 (mean±SD, n=49 cells). In contrast, significantly higher, positive rel.3C. values were obtained
628 for the polymerase samples, rel.3C.=0.43±0.38 (mean±SD, n=53 cells). The detection of
629 ternary complexes is limited by non-fluorescent FPs, i.e. only a fraction of ternary complexes

present in a sample will emit coincident signals for all three FP species. In addition, imperfect overlap of the detection volumes for each channel will further reduce the fraction of ternary complexes that can be detected by TRICS. We therefore performed an approximate calculation of the expected rel.3C. value for a sample containing 100% ternary complexes assuming a $p_f$ of 0.7 for each FP species and estimating the reduction due to imperfect overlap from the pair-wise rel.cc. values detected on the positive cross-correlation control (see Appendix, paragraph 3 for details). For a 2:2:2 stoichiometry, we obtained an estimated rel.3C. of 0.48, i.e. only slightly higher than the average value determined experimentally for IAV PCs. Thus, we estimate that around 90% of PC subunits undergo ternary complex formation in the cell nucleus when all subunits are present.

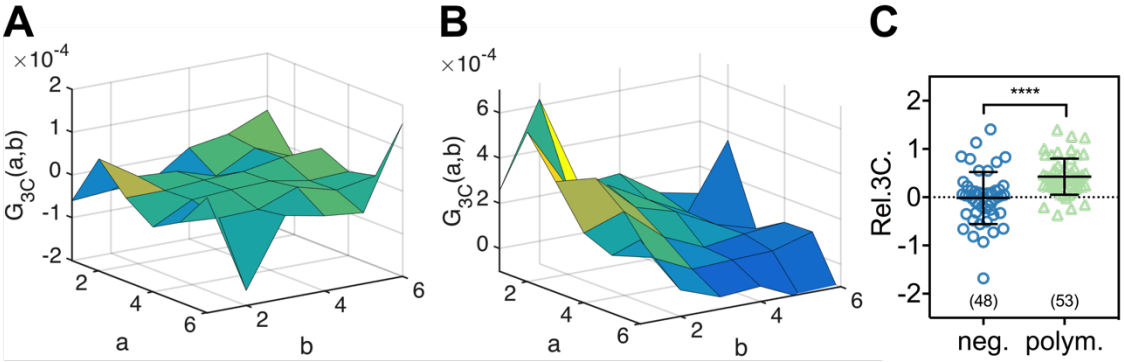


**Figure 7. TRICS reveals the formation of ternary IAV polymerase hetero-complexes in the nucleus of A549 cells. (A,B)** Representative 3CFs obtained from TRICS measurements on A549 cells co-expressing mEGFP, mEYFP, and mCherry2 ("neg.") (A) or co-expressing PA-mEYFP, PB1-mEGFP, and PB2-mCherry2 ("polym.") (B). The axes *a* and *b* indicate shifts in the x and y direction respectively, across the three detection channels, as described in the Materials and Methods. (C) Relative triple-correlation (rel.3C.) values obtained from the measurements described in (A,B). The number of cells measured is given in parentheses. Error bars represent mean±SD. Statistical significance was determined using Welch's corrected two-tailed student's *t*-test (****$P$<0.0001).

653 **DISCUSSION**

654 In this work, we combine FFS techniques with spectral detection to perform multi-color studies
655 of protein interactions and dynamics in living cells. In particular, we present SFSCS, a
656 combination of FSCS (22) and lateral scanning FCS (11). We show that SFSCS allows cross-
657 talk-free measurements of protein interactions and diffusion dynamics at the PM of cells and
658 demonstrate that it is capable of detecting three or four species simultaneously. Furthermore,
659 we extend RSICS (27) to investigate four fluorophore species and apply this approach to
660 determine the stoichiometry of higher order protein complexes assembling in the cell nucleus.
661 Notably, the technical approaches can be carried out on a standard confocal microscope,
662 equipped with a spectral photon counting detector system.

663 In the first part, we present two-species SFSCS using a single excitation wavelength and
664 strongly overlapping fluorophores. Compared to the conventional implementation of FCCS
665 with two excitation lasers and two detectors, two-species SFSCS has substantial advantages,
666 similar to the recently presented sc-FLCCS (28). Since it requires a single excitation line and
667 is compatible with spectrally strongly overlapping FPs, it circumvents optical limitations such
668 as imperfect overlap of the observation volumes. This is evident from higher rel.cc. values of
669 70-80% measured for mEGFP and mEYFP coupled in FP hetero-oligomers compared to 45-
670 60% observed for mEGFP and mCherry2. Rel.cc. values around 70% are to be expected for the
671 examined FP tandems even in the case of single-wavelength excitation, given that the $p_f$ for
672 such fluorophores is indeed around 0.7 (14, 29) (see also SI, paragraph 1). On the other hand,
673 in three- and four species measurements discussed below, FP pairs requiring two excitation
674 wavelengths display the typical reduction of the rel.cc. due to imperfect optical volume overlap.
675 For combinations of green and red FPs rel.cc. values below 60% were also observed with
676 single-wavelength excitation (29, 38), indicating that overlap of both excitation and detection
677 volumes (the latter requiring FPs with similar emission spectra) is required to maximize the

678 achievable cross-correlation (29). Notably, two-species SFSCS can not only successfully
679 discriminate between mEGFP and mEYFP, but is also applicable when using the red FPs
680 mApple and mCherry2. These two FPs were successfully used in several FFS studies (14, 30,
681 39), providing the best compromise between brightness, maturation and photostability among
682 available red FPs, which generally suffer from reduced SNR compared to FPs emitting in the
683 green or yellow part of the optical spectrum (13, 14, 40).
684 In comparison to sc-FLCCS, it may be more robust to discriminate fluorophores based on
685 spectra rather than lifetimes, which can be strongly affected by FRET (28). The emission
686 spectra of the FPs utilized in this study did not depend on cell lines or subcellular localization
687 (Figure 5-figure supplement 1) and showed no (mEGFP, mEYFP) or little (mApple, mCherry2)
688 variation with pH over a range of 5.0 to 9.2. (Figure 5-figure supplement 2). For red FPs,
689 specifically mApple, a red shift appeared at more acidic pH, in agreement with previous studies
690 (41). This aspect should be considered for specific applications, e.g. RSICS in the cytoplasm
691 containing acidic compartments such as lysosomes. Generally, spectral approaches require
692 accurate detection of photons in each spectral bin. A previous study using the same detection
693 system reported intrinsic cross-talk between adjacent spectral bins (30). However, since the
694 methodology presented here is based on temporal (SFSCS) or spatial (RSICS) correlation (both
695 excluding the correlation at zero time or spatial lag), this issue can be neglected in our analysis.
696 A major limitation of SFSCS is the reduced SNR of the CFs (see Fig.1, Figure 3-figure
697 supplement 3) caused by the statistical filtering of the signal emitted by spectrally overlapping
698 fluorophore species (see e.g. Figure 4-figure supplement 1). This limitation applies to all FFS
699 methods that discriminate different fluorophore species based on spectral (e.g. FSCS (22),
700 RSICS (27)) or lifetime patterns (e.g. sc-FLCCS (28)). The increase in noise depends on the
701 spectral (or lifetime) overlap of different species and is more prominent for species that
702 completely lack “pure” channels, i.e. detection channels in which the majority of photons can
703 be univocally assigned to a single species (27). In sc-FLCCS, this issue particularly

704 compromises the SNR of short lifetime species (28), since photons of longer lifetime species
705 are detected in all "short lifetime" channels at substantial relative numbers. In these conditions,
706 sc-FLCCS could not provide reliable results with 6-fold (or higher) difference in relative protein
707 abundance, even though the lower abundant protein was tagged with the brighter, longer
708 lifetime FP (28). Similarly in SFSCS, CFs corresponding to mEYFP or mCherry2 were most
709 prone to noise (Fig.1C,F), since all channels that contain, e.g., mEYFP signal also contain
710 mEGFP signal (Figure 1-figure supplement 1). In our experiments, cross-talk-free SFSCS
711 analysis with two species excited with a single excitation wavelength could be performed for
712 relative intensity levels as low as 1:10 (mEGFP/mEYFP) or 1:5 (mApple/mCherry2). In this
713 range, SFSCS not only enabled the quantification of protein interactions via cross-correlation
714 analysis, but also yielded correct estimates of protein diffusion dynamics and oligomerization
715 at the PM. An improvement of the allowed relative concentration range can be achieved by
716 using brighter or more photostable fluorophores, e.g. organic dyes, compensating for reduced
717 SNR due to statistical filtering. Alternatively, FP tags could be selected based on proteins
718 oligomerization state, e.g. monomeric proteins exhibiting low molecular brightness should be
719 tagged with fluorophores that are less prone to noise. It should be noted that the limitation of
720 reduced SNR due to excess signal from another species also applies to conventional dual-color
721 FCCS: bleed-through from green to red channels can be corrected on average, but reduces the
722 SNR in red channels (42), unless more sophisticated schemes such as pulsed interleaved
723 excitation (43, 44) are applied.
724 Having demonstrated that two-species SFSCS is feasible with a single excitation wavelength
725 in the green (mEGFP, mEYFP) or red (mApple, mCherry2) part of the visible spectrum, we
726 finally implemented three- and four-species SFSCS as well as four-species RSICS. Three- and
727 four-species SFSCS/ RSICS do not further compromise the SNR of CFs detected for mEGFP
728 and mEYFP (see Figure 3-figure supplement 3A,B), but may additionally reduce the SNR of
729 CFs corresponding to red FPs (in particular when mEGFP and/ or mEYFP concentration is

730 much higher than that of red FPs, Figure 3-figure supplement 3C). For this reason, three- and
731 four-species analysis was restricted to cells with relative average intensity levels of 1:5 or less
732 between species with adjacent emission spectra. In this range, the increase in noise due to
733 statistical filtering was moderate and benefited from the fairly large spectral separation of
734 green/yellow and red emission (Figure 3-figure supplement 3). In addition, the higher molecular
735 brightness of mApple (compared to mCherry2) compensated for the larger overlap of this FP
736 with the tail of mEYFP emission. The excitation power for red FPs was generally limited by
737 the lower photostability of mApple, which could be responsible for consistently lower rel.cc.
738 values of mEGFP or mEYFP with mApple than with mCherry2. Nevertheless, four-species
739 SFSCS and RSICS could successfully resolve different combinations of strongly overlapping
740 FP hetero-oligomers, e.g. a mixture of mEGFP-mCherry2 and mEYFP-mApple hetero-dimers,
741 at the PM or in the cytoplasm of cells. To explore the interaction of four different FP-tagged
742 proteins, four-species FFS may substantially reduce the experimental effort, because all pair-
743 wise interactions can be quantified in a single measurement (instead of six separate
744 conventional two-species FCCS measurements). Yet, weak interaction of proteins, i.e. a low
745 amount of hetero-complexes compared to a high amount of unbound proteins, may not be
746 detectable, due to the large noise of the CCF in this case. The SNR might be further
747 compromised by slow FP maturation or dark FP states, limiting the amount of complexes that
748 simultaneously emit fluorescence of all bound FP species (14). Ultimately, the mentioned
749 limitations currently restrict SFSCS and RSICS to four FP species. The approaches would thus
750 strongly benefit from a multiparametric analysis. For instance, combining spectral and lifetime
751 detection schemes would provide additional contrast for photons detected in the same spectral
752 bin. This improvement could expand the range of detectable relative concentrations or might
753 allow further multiplexing of FFS.
754 Conventional two-color scanning FCCS has been previously applied to quantify receptor-ligand
755 interactions in living zebrafish embryos (12) and CRISPR/Cas9 edited cell lines to study such

756 interactions at endogenous protein level (45). SFSCS is thus directly applicable in the complex
757 environment of living multicellular organisms. In this context, spectral information could be
758 further exploited to separate low signal levels of endogenously expressed, fluorescently tagged
759 proteins from autofluorescence background.
760 As a first biological application of SFSCS, we investigated the interaction of IAV matrix protein
761 M2 with two cellular host factors: the tetraspanin CD9 and the autophagosome protein LC3.
762 We observed strong association of LC3 with M2, and consequent recruitment of LC3 to the PM
763 (Figure 3-figure supplement 4), in agreement with previous *in vitro* and localization studies
764 (34). Interestingly, molecular brightness analysis reported oligomerization (dimers to
765 tetramers) of M2, but indicated a monomeric state of LC3 at the PM, i.e. binding of LC3 to M2
766 in an apparent stoichiometry of 1:2 to 1:4. However, each M2 monomer provides a binding site
767 for LC3 in the cytoplasmic tail (46). A more detailed analysis of our data showed that in the
768 analyzed cells (i.e. cells showing clear membrane recruitment of LC3, Figure 3-figure
769 supplement 4A,B), the PM concentration of LC3 was on average only 30% compared to that of
770 M2 (Figure 3-figure supplement 4C), although both proteins were expressed in comparable
771 amounts in the sample in general. This suggests that not all potential binding sites in the
772 cytoplasmic tail of M2 may be available to fluorescently tagged LC3, either due to binding of
773 endogenous LC3, other cellular host factors, or steric hindrance. In contrast to the case of LC3,
774 we did not detect significant binding of M2 with the tetraspanin CD9, a protein that was
775 previously shown to be incorporated into IAV virions and supposedly plays a functional role
776 during the infection process (47, 48). Of note, we cannot exclude the possibility that the FP tag
777 at the C-terminus of CD9 might hamper interactions with M2, in the specific case of M2-CD9
778 interaction being mediated by the C-terminal cytoplasmic tails of the two proteins. In future
779 studies, the approach presented here may be used to further elucidate the complex interaction
780 network of viral proteins, e.g. matrix protein 1 (M1) (49), M2, HA, and neuraminidase, cellular

781 host factors, and PM lipids (50) during the assembly process of IAV at the PM of living cells
782 (51).
783 Finally, we demonstrated that RSICS allows the quantification of the stoichiometry of higher
784 order molecular complexes, based on molecular brightness analysis for each FP species. As
785 example of an application in a biological context, we determined the stoichiometry of the IAV
786 PC. Our data provide strong evidence for a 2:2:2 stoichiometry of the PC subunits PA, PB1 and
787 PB2, i.e. dimerization of hetero-trimeric PCs. Such interactions were previously proposed
788 based on experiments in solution using X-ray crystallography and cryo-electron microscopy
789 (52), co-immunoprecipitation assays (53, 54), as well as single channel brightness analysis of
790 FCCS data (for the PA subunit) (36). Intermolecular interactions in the PC are hypothesized to
791 be required for the initiation of vRNA synthesis during replication of the viral genome (52, 55).
792 The results presented here provide the first quantification of these interactions in living cells,
793 and a direct estimate of the stoichiometry of PCs in the cell nucleus. The formation of ternary
794 PC complexes in these samples could be extrapolated from the observed high rel.cc. values for
795 all three pair combinations, indicating very low amounts of unbound PA, PB1 or PB2 and
796 higher order interactions (see Appendix, paragraph 1 for additional details). Furthermore, this
797 observation could also be directly confirmed by performing, for the first time in living cells, a
798 triple correlation analysis (TRICS), indicating the presence of a considerable amount of PA-
799 PB1-PB2 complexes. It is worth noting though that the detection of coincident triple
800 fluctuations is prone to considerable noise and thus still limited to molecular complexes present
801 at low concentration and characterized by high molecular brightness for each fluorophore
802 species (21, 56).
803 Of note, the RSICS approach presented here provides for the first time simultaneous
804 information on molecular interactions, molecular brightness (and thus stoichiometry), diffusion
805 dynamics, and concentration for all three complex subunits. This specific feature opens the
806 possibility of a more in-depth analysis. For example, it is possible to quantify the relative cross-

807 correlation of two subunits, e.g. PA and PB2, as a function of the relative concentration of the
808 third subunit, e.g. PB1 (Figure 6-figure supplement 1A). Similarly, molecular brightness and
809 diffusion coefficients can be analyzed as a function of the abundance of each subunit (Figure
810 6-figure supplement 1B,C). With this approach, it is therefore possible to distinguish specific
811 molecular mechanism, e.g. inefficient PA-PB2 interactions in the presence of low PB1
812 concentration or efficient hetero-trimer dimerization when all subunits are present at similar
813 concentrations. The employed experimental scheme offers a powerful tool for future studies,
814 exploring, for example, interaction of the PC with cellular host factors or the development of
815 inhibitors that could interfere with the assembly process of the complex, as a promising
816 therapeutic target for antiviral drugs (57).
817

818 ## Limitations

819 We summarize in this section the main instrumental, conceptual and sample-related limitations
820 and requirements connected to the multi-color FFS approach employed in this work.

821 **Instrumental limitations**

822 To perform multi-color FFS, a spectral photon counting detector system is required.
823 Alternatively, the same conceptual approach can be implemented based on detection of
824 fluorophore lifetimes rather than emission spectra (28). For both approaches, two excitation
825 wavelengths are currently required for three- and four-species detection. As a consequence, the
826 overlap of excitation volumes of the two laser lines might be limited, thus reducing the
827 maximum achievable rel.cc., as previously discussed for standard FCCS (29). For the
828 instrumentation utilized in the present work, the time resolution for SFSCS was limited to 0.5
829 ms. However, RSICS can be applied to detect faster dynamics, as demonstrated by experiments
830 on cytoplasmic proteins.

831 **Conceptual limitations**

832 FFS approaches generally require the proteins of interest to diffuse and thus cannot be applied
833 in the case of immobile or strongly clustered targets (58). The statistical filtering of spectrally
834 overlapping FP emission leads to increased noise of CFs. FPs lacking "pure" channels, e.g.
835 mEYFP when co-expressed with mEGFP, are most compromised. As a consequence, the
836 approach provides reliable results only in a certain range of relative protein abundance. For the
837 presented three- and four-species SFSCS and RSICS experiments, relative signals were limited
838 to 1:5 (i.e. range of 1:5 to 5:1). The given ratios characterize the minimum acceptable signal
839 ratio for spectrally neighboring fluorescent species, for the FPs utilized in this work. The set of
840 FPs may be optimized for specific applications. The increase in noise as a result of filtering
841 may prevent detection of weak protein interactions, due to the low SNR of CCFs in this case.
842 Furthermore, detection of co-fluctuations of three FP species based on triple correlation is prone
843 to considerable noise and thus limited to detection of molecular complexes present at low
844 concentrations or characterized by high molecular brightness, as discussed previously for *in*
845 *vitro* studies (21).

846 **Sample-related limitations**

847 To apply multi-color FFS, multiple FP species (e.g. FP-tagged proteins of interest) have to be
848 expressed in the same cell, in relative amounts compatible with the ranges given above. Since
849 tagging of proteins of interest with FPs is required (or other labels such as organic dyes, if the
850 labelling ratio can be precisely determined), potential hindrance of protein interactions by the
851 tags should be carefully evaluated. Typical measures consist in e.g. testing different positions
852 for the tag in the protein of interest, trying different linkers with varying length and flexibility,
853 using tags with smaller sizes, or e.g. bio-orthogonal labeling (59, 60). The emission spectra of
854 most FPs are typically well-defined, but might depend on physicochemical conditions (e.g.

855 mApple shows red-shifted emission at more acidic pH). Differences between calibrated and
856 actual spectra could induce errors in filtering and cause residual cross-talk between different
857 FP species. Therefore, the same optical components (e.g. filters, beam splitters) and
858 experimental conditions (e.g. laser powers, sample media, dishes) should be used to calibrate
859 the spectra. Due to lower photostability and quantum yield, red FPs suffer from reduced SNR
860 and, thus, larger variation of parameter estimates compared to green FPs. This is most evident
861 for mCherry2 in four-species applications. In addition, molecular brightness and cross-
862 correlation analysis are compromised by FP maturation. Slow maturation will lead to an
863 increased fraction of dark states, increasing the noise of CCFs and reducing the dynamic range
864 for brightness analysis of protein oligomers (14, 29). Cross-correlation analysis may be further
865 affected by FRET between different FP species, potentially reducing experimental rel.cc. values
866 (29). This should be carefully evaluated, e.g. by analyzing molecular brightness values relative
867 to monomeric references, for both the proteins of interest and FP-hetero-oligomers used to
868 calibrate the maximum achievable rel.cc.. FRET artefacts can be minimized using appropriate
869 linkers, e.g. rigid linker peptides, as presented here.

870

871 **Conclusions**

872 In summary, we present here three-species and, for the first time, four-species measurements
873 of protein interactions and diffusion dynamics in living cells. This is achieved by combining
874 and extending existing FFS techniques with spectrally resolved detection. The presented
875 approaches provide a powerful toolbox to investigate complex protein interaction networks in
876 living cells and organisms.

877

878 # MATERIALS AND METHODS

879 ## Cell culture and sample preparation

880 Human embryonic kidney (HEK) cells from the 293T line (purchased from ATCC®, Manassas,
881 VA, USA, CRL-3216TM) and human epithelial lung cells A549 (ATCC®, CCL-185TM) were
882 cultured in Dulbecco's modified Eagle medium (DMEM) with the addition of fetal bovine
883 serum (10%) and L-Glutamine (2 mM). Mycoplasma contamination tests and morphology tests
884 were performed every 3 months and 2 weeks, respectively. Cells were passaged every 3–5 days,
885 no more than 15 times. All solutions, buffers and media used for cell culture were purchased
886 from PAN-Biotech (Aidenbach, Germany).
887 For microscopy experiments, $3 \times 10^5$ (HEK) or $4 \times 10^5$ (A549) cells were seeded in 35 mm
888 #1.5 optical glass bottom dishes (CellVis, Mountain View, CA, USA) 24 h before transfection.
889 Cells were transfected 16–24 h prior to the experiment using between 50 ng and 150 ng plasmid
890 per dish with Turbofect (HEK) or Lipofectamin3000 (A549) according to the manufacturer's
891 instructions (Thermo Fisher Scientific, Waltham, MA, USA). Briefly, plasmids were incubated
892 for 20 min with 3 µl Turbofect diluted in 50 µl serum-free medium, or 15 min with 2 µl P3000
893 and 2 µl Lipofectamine3000 diluted in 100 µl serum-free medium, and then added dropwise to
894 the cells. For spectral imaging at different pH values, culture medium was exchanged with
895 buffer containing 140 mM NaCl, 2.5 mM KCl, 1.8 mM $CaCl_2$, 1.0 mM $MgCl_2$, and 20 mM
896 HEPES with pH ranging from 5.0 to 9.2.
897

898 ## Plasmids and cloning

899 The plasmids encoding FPs linked to a myristoylated and palmitoylated peptide (mp-mEGFP,
900 mp-mEYFP, mp-mCherry2, mp-2x-mEGFP), the full length IAV A/chicken/FPV/Rostock/
901 1934 hemagglutinin (HA) construct HA-mEGFP, and the plasmids for cytosolic expression of

902 mEGFP, mEYFP, mCherry2, 2x-mEGFP, 2x-mEYFP, 2x-mCherry2 and mCherry2-mEGFP
903 hetero-dimers were previously described (14) and are available on Addgene.
904 For the cloning of all following constructs, standard PCRs with custom-designed primers were
905 performed, followed by digestion with fast digest restriction enzymes and ligation with T4-
906 DNA-Ligase according to the manufacturer's instructions. All enzymes and reagents were
907 purchased from Thermo Fisher Scientific, Waltham, MA, USA.
908 To obtain mp-mEGFP-mEYFP, a mp-mEGFP_pcDNA3.1+ vector was first generated by
909 amplifying mp-mEGFP insert from the respective plasmid, and inserting it into pcDNA3.1+
910 vector (obtained from Thermo Fisher Scientific ) by digestion with NheI and AflII. Afterwards,
911 mEYFP was amplified from mp-mEYFP, and inserted into mp-mEGFP_pcDNA3.1+ using
912 digestion with AflII and KpnI. To clone mp-mEYFP-(L)-mEGFP (a plasmid encoding for mp-
913 mEYFP-mEGFP hetero-dimers with a long rigid linker peptide (L) between FPs), a mp-
914 mEYFP-(L)_pcDNA3.1+ construct was first generated by amplifying mp-mEYFP from the
915 respective plasmid with primers encoding for the rigid linker (see supplementary file 1a for
916 linker peptide sequences) and inserting it into pcDNA3.1+ vector by digestion with NheI and
917 AflII. Then, mEGFP was inserted from mEGFP-(L)_pcDNA3.1+ (see below) by digestion with
918 KpnI and BamHI. To generate mp-mEYFP-(L)-mCherry2-(L)-mEGFP, a mp-mEYFP-(L)-
919 mCherry2-(L) construct was first cloned by amplifying mCherry2 from a mCherry2-C1 vector
920 (a gift from Michael Davidson, Addgene plasmid # 54563) and inserting it into mp-mEYFP-
921 (L)_pcDNA3.1+ by digestion with AflII and KpnI. Subsequently, mEGFP was inserted from
922 mEGFP-(L)_pcDNA3.1+ (see below) using KpnI and BamHI restriction. The mp-mEYFP-(L)-
923 mCherry2-(L)-mEGFP-(L)-mApple plasmid was generated by inserting an mEGFP-(L)-
924 mApple cassette into mp-mEYFP-(L)-mCherry2-(L) by digestion with KpnI and EcoRI. The
925 mEGFP-(L)-mApple construct was cloned beforehand by amplifying mApple from PMT-
926 mApple (39) (a kind gift from Thorsten Wohland) and inserting it into mEGFP-
927 (L)_pcDNA3.1+ by digestion with BamHI and EcoRI. The mEGFP-(L)_pcDNA3.1+ plasmid

928 was obtained by amplifying mEGFP from an mEGFP-N1 vector (a gift from Michael Davidson,
929 Addgene plasmid # 54767) (using a primer encoding a long rigid linker sequence) and inserting
930 it into a pcDNA3.1+ vector by KpnI and BamHI restriction. The mApple_pcDNA3.1+ plasmid
931 was generated by amplifying mApple from PMT-mApple and inserting it into pcDNA3.1+
932 vector by digestion with KpnI and BamHI. The mp-mApple plasmid was generated by
933 amplifying mApple from PMT-mApple, and inserting it into mp-mCherry2 by digestion with
934 AgeI and BsrGI. To clone mp-mCherry2-(L)-mApple, a mp-mCherry2-(L)_pcDNA3.1+
935 plasmid was first generated by amplifying mp-mCherry2 (using a primer encoding a long rigid
936 linker sequence) and inserting it into pcDNA3.1+ using NheI and KpnI restriction. Afterwards,
937 mApple was amplified from PMT-mApple and inserted into mp-mCherry2-(L)_pcDNA3.1+
938 by digestion with KpnI and EcoRI. The mp-mCherry2-mEGFP plasmid was cloned by inserting
939 mp from mp-mEGFP into mCherry2-mEGFP, using digestion with NheI und AgeI. The
940 plasmids mEYFP-(L)-mApple, mEYFP-(L)-mCherry2-(L)-mEGFP and mEYFP-(L)-
941 mCherry2-(L)-mEGFP-(L)-mApple were generated by amplifying the respective insert from
942 mp-mEYFP-(L)-mApple, mp-mEYFP-(L)-mCherry2-(L)-mEGFP or mp-mEYFP-(L)-
943 mCherry2-(L)-mEGFP-(L)-mApple and inserting it into pcDNA3.1+ vector by digestion with
944 NheI and XbaI. The mp-mEYFP-(L)-mApple construct was cloned beforehand by inserting
945 mApple from mEGFP-(L)-mApple into mp-mEYFP-(L)_pcDNA3.1+ using restriction by
946 BamHI and EcoRI.

947 The CD9-mEGFP plasmid was cloned by amplifying CD9 from pCMV3-CD9 (obtained from
948 SinoBiological #HG11029-UT, encoding human CD9) and inserting into an mEGFP-C1 vector
949 using restriction by HindIII and BamHI. The LC3-mEYFP plasmid was generated by inserting
950 mEYFP from an mEYFP-C1 vector into pmRFP-LC3 (61) (a gift from Tamotsu Yoshimori,
951 Addgene plasmid # 21075, encoding rat LC3) using digestion with NheI and BglII. Plasmid
952 M2-mCherry2 (mCherry2 fused to the extracellular terminus of matrix protein 2 from influenza

953 A/chicken/FPV/Rostock/1934) was cloned by inserting mCherry2 from an mCherry2-C1
954 vector into mEYFP-FPV-M2 (a kind gift from Michael Veit) using restriction by AgeI and
955 BsrGI. Plasmids encoding IAV polymerase subunits PA-mEYFP, PB1-mEGFP and PB2-
956 mCherry2 (from influenza A/human/WSN/1933) were a kind gift from Andreas Herrmann.
957 The plasmids GPI-mEYFP and GPI-EGFP were a kind gift from Roland Schwarzer. GPI-
958 mEGFP was cloned by amplifying mEGFP from an mEGFP-N1 vector and inserting it into
959 GPI-EGFP, using digestion with AgeI and BsrGI. To generate GPI-mApple and GPI-
960 mCherry2, mApple and mCherry2 inserts were amplified from PMT-mApple and mCherry2-
961 C1, respectively, and inserted into GPI-mEYFP using restriction by AgeI and BsrGI.

962 All plasmids generated in this work will be made available on Addgene.

963

964 **Confocal microscopy system**

965 Scanning fluorescence spectral correlation spectroscopy (SFSCS) and raster spectral image
966 correlation spectroscopy (RSICS) were performed on a Zeiss LSM880 system (Carl Zeiss,
967 Oberkochen, Germany) using a 40x, 1.2NA water immersion objective. For two-species
968 measurements, samples were excited with a 488 nm Argon laser (mEGFP, mEYFP) or a 561
969 nm diode laser (mCherry2, mApple). For three- and four-species measurements, both laser lines
970 were used. To split excitation and emission light, 488 nm (for two-species measurements with
971 mEGFP and mEYFP) or 488/561 nm (for measurements including mCherry2 and mApple)
972 dichroic mirrors were used. Fluorescence was detected in spectral channels of 8.9 nm (15
973 channels between 491 nm and 624 nm for two-species measurements on mEGFP, mEYFP; 14
974 channels between 571 nm and 695 nm for two-species measurements on mCherry2, mApple;
975 23 channels between 491 nm and 695 nm for three- and four-species measurements) on a 32
976 channel GaAsP array detector operating in photon counting mode. All measurements were
977 performed at room temperature.

978

979 **Scanning fluorescence spectral correlation spectroscopy (SFSCS)**

980 *Data acquisition*: For SFSCS measurements, a line scan of 256x1 pixels (pixel size 80 nm) was
981 performed perpendicular to the PM with 403.20 µs scan time. This time resolution is sufficient
982 to reliably detect the diffusion dynamics observed in the samples described in this work (i.e.
983 diffusion times ~6-60 ms). Typically, 450,000-600,000 lines were acquired (total scan time ca.
984 2.5 to 4 min). Laser powers were adjusted to keep photobleaching below 50% at maximum for
985 all species (average signal decays were ca. 10% for mEGFP, 30% for mEYFP, 40% for mApple
986 and 20% for mCherry2). Typical excitation powers were ca. 5.6 µW (488 nm) and ca. 5.9 µW
987 (561 nm). Spectral scanning data were exported as TIFF files (one file per three spectral
988 channels), imported and analyzed in MATLAB (The MathWorks, Natick, MA, USA) using
989 custom-written code (62).

990 *Data analysis*: SFSCS analysis followed the scanning FCS scheme described previously (11,
991 63), combined with spectral decomposition of the fluorescence signal by applying the
992 mathematical framework of FLCS and FSCS (22, 23). Briefly, all scan lines were aligned as
993 kymographs and divided in blocks of 1000 lines. In each block, lines were summed up column-
994 wise and across all spectral channels, and the lateral position with maximum fluorescence was
995 determined. This position defines the membrane position in each block and was used to align
996 all lines to a common origin. Then, all aligned line scans were averaged over time and fitted
997 with a Gaussian function. The pixels corresponding to the PM were defined as pixels within ±
998 2.5SD of the peak. In each line and spectral channel these pixels were integrated, providing
999 membrane fluorescence time series $F^k(t)$ in each spectral channel $k$ ($m$ channels in total). These
1000 time series were then temporally binned with a binning factor of two and subsequently
1001 transformed into the contributions $F_i(t)$ of each fluorophore species $i$ (i.e. one fluorescence

time series for each species) by applying the spectral filtering algorithm presented by Benda et al. (22):

$$F_i(t) = \sum_{k=1}^{m} f_i^k F^k(t).$$

Spectral filter functions $f_i^k$ were calculated based on reference emission spectra $p_i^k$ that were determined for each individual species *i* from single species measurements performed on each day, using the same acquisition settings:

$$f_i^k = \left(\left[\widehat{M}^T D \widehat{M}\right]^{-1} \widehat{M} D\right)_{ik}.$$

Here, $\widehat{M}$ is a matrix with elements $M_{ki} = p_i^k$ and *D* is a diagonal matrix, $D = diag[1/\langle F^k(t)\rangle]$. In order to correct for depletion due to photobleaching, a two-component exponential function was fitted to the fluorescence time series for each spectral species, $F_i(t)$, and a correction formula was applied (63, 64). Finally, autocorrelation functions (ACFs) and pair-wise cross-correlation functions (CCFs) of fluorescence time series of species *i* and *j* were calculated as follows, using a multiple tau algorithm:

$$G_i(\tau) = \frac{\langle \delta F_i(t) \delta F_i(t+\tau)\rangle}{\langle F_i(t)\rangle^2},$$

$$G_{i,j}(\tau) = \frac{\langle \delta F_i(t) \delta F_j(t+\tau)\rangle}{\langle F_i(t)\rangle \langle F_j(t)\rangle},$$

where $\delta F_i(t) = F_i(t) - \langle F_i(t)\rangle$.

To avoid artefacts caused by long-term instabilities or single bright events, CFs were calculated segment-wise (10-20 segments) and then averaged. Segments showing clear distortions (typically less than 25% of all segments) were manually removed from the analysis (63).

A model for two-dimensional diffusion in the membrane and Gaussian focal volume geometry (11) was fitted to all CFs:

$$G(\tau) = \frac{1}{N}\left(1 + \frac{\tau}{\tau_d}\right)^{-1/2}\left(1 + \frac{\tau}{\tau_d S^2}\right)^{-1/2}$$

To ensure convergence of the fit for all samples (i.e. ACFs and CCFs of correlated and un-correlated data), positive initial fit values for the particle number *N* and thus $G(\tau)$ were used.

1026 In the case of uncorrelated data, i.e. for CFs fluctuating around zero, this constraint can generate
1027 low, but positive correlation amplitudes due to noise. This issue can be circumvented, if needed,
1028 by selecting adaptive initial values, e.g. obtaining the initial amplitude value from averaging
1029 the first points of the CFs (see Figure 3-figure supplement 2).
1030 To calibrate the focal volume, point FCS measurements with Alexa Fluor® 488 (Thermo Fisher
1031 Scientific, Waltham, MA, USA) dissolved in water at 20 nM were performed at the same laser
1032 power. The structure parameter $S$ was fixed to the average value determined in calibration
1033 measurements (typically between 4 to 8).
1034 From the amplitudes of ACFs and CCFs, relative cross-correlation (rel.cc.) values were
1035 calculated for all cross-correlation combinations:

1036 $$rel.cc._{i,j} = max\left\{\frac{G_{i,j}(0)}{G_i(0)}, \frac{G_{i,j}(0)}{G_j(0)}\right\},$$

1037
1038 where $G_{i,j}(0)$ is the amplitude of the CCF of species $i$ and $j$, and $G_i(0)$ the amplitude of the ACF
1039 of species $i$. The molecular brightness was calculated by dividing the mean count rate detected
1040 for each species $i$ by the particle number $N_i$ determined from the fit: $B_i = \frac{\langle F_i(t)\rangle}{N_i}$. From this
1041 value, an estimate of the oligomeric state $\varepsilon_i$ was determined by normalizing $B_i$ by the average
1042 molecular brightness $B_{i,1}$ of the corresponding monomeric reference, and, subsequently, by the
1043 fluorescence probability $p_{f,i}$ for species $i$: $\varepsilon_i = \frac{\frac{B_i}{B_{i,1}}-1}{p_{f,i}} + 1$, as previously derived (14). The $p_f$ was
1044 previously characterized for several FPs, e.g. ca. 60% for mCherry2 (14).
1045 The signal-to-noise ratio (SNR) of the ACFs was calculated by dividing ACF values by their
1046 variance and summing over all points of the ACF. The variance of each point of the ACF was
1047 calculated in the multiple tau algorithm (65).
1048 To ensure statistical robustness of the SFSCS analysis and sufficient SNR, the analysis was
1049 restricted to cells expressing all fluorophore species in comparable amounts, i.e. relative

1050 average signal intensities of less than 1:10 (mEGFP/mEYFP) or 1:5 (mApple/mCherry2, three-
1051 and four-species measurements).
1052
1053 **Raster spectral image correlation spectroscopy (RSICS)**
1054 *Data acquisition:* RSICS measurements were performed as previously described (66). Briefly,
1055 200-400 frames of 256x256 pixels were acquired with 50 nm pixel size (i.e. a scan area of
1056 12.83x12.83 $\mu m^2$ through the midplane of cells), 2.05 µs or 4.10 µs pixel dwell time, 1.23 ms
1057 or 2.46 ms line, and 314.57 ms or 629.14 ms frame time (corresponding to ca. 2 min total
1058 acquisition time per measurement). Samples were excited at ca. 5.6 µW (488 nm) and 4.6 µW
1059 (561 nm) excitation powers, respectively. Laser powers were chosen to maximize the signal
1060 emitted by each fluorophore species but keeping photobleaching below 50% at maximum for
1061 all species (average signal decays were ca. 10% for mEGFP, 15% for mEYFP, 40% for mApple
1062 and 25% for mCherry2). Typical counts per molecule were ca. 25 kHz for mEGFP (G), 15-20
1063 kHz for mEYFP (Y), 20-30 kHz for mApple (A), and 5-10 kHz for mCherry2 (Ch2). To obtain
1064 reference emission spectra for each individual fluorophore species, four image stacks of 25
1065 frames were acquired at the same imaging settings on single species samples on each day.
1066 *Data analysis:* RSICS analysis followed the implementation introduced recently (27), which is
1067 based on applying the mathematical framework of FLCS and FSCS (22, 23) to RICS. Four-
1068 dimensional image stacks $I(x, y, t, k)$ (time-lapse images acquired in $k$ spectral channels) were
1069 imported in MATLAB (The MathWorks, Natick, MA, USA) from CZI image files using the
1070 Bioformats package (67) and further analyzed using custom-written code (62). First, average
1071 reference emission spectra were calculated for each individual fluorophore species from single-
1072 species measurements. Four-dimensional image stacks were then decomposed into three-
1073 dimensional image stacks $I_i(x, y, t)$ for each species $i$ using the spectral filtering algorithm
1074 presented by Schrimpf et al. (27) (following the mathematical framework given in the SFSCS
1075 section). Cross-correlation RICS analysis was performed in the arbitrary region RICS

1076 framework (35). To this aim, a polygonal region of interest (ROI) was selected in the time- and
1077 channel-averaged image frame containing a homogeneous region in the cytoplasm (four-
1078 species measurements on FP constructs) or nucleus (three-species measurements on polymerase
1079 complex and related controls) of cells. This approach allowed excluding visible intracellular
1080 organelles or pixels in the extracellular space, but to include all pixels containing signal from
1081 the nucleus of cells. In some cells, nucleus and cytoplasm could not be clearly distinguished.
1082 In these cases, all pixels were selected and minor brightness differences between cytoplasm and
1083 nucleus, previously found to be ca. 10% (14), were neglected. Image stacks were further
1084 processed with a high-pass filter (with a moving 4-frame window) to remove slow signal
1085 variations and spatial inhomogeneities. Afterwards, RICS spatial ACFs and pair-wise CCFs
1086 were calculated for each image stack and all combinations of species *i, j* (e.g. G and Y, G and
1087 Ch2, Y and Ch2 for three species), respectively (27, 35):

1088 $$G_i(\xi,\psi) = \frac{\langle \delta I_i(x,y)\delta I_i(x+\xi,y+\psi)\rangle}{\langle I_i(x,y)\rangle^2},$$

1089 $$G_{i,j}(\xi,\psi) = \frac{\langle \delta I_i(x,y)\delta I_j(x+\xi,y+\psi)\rangle}{\langle I_i(x,y)\rangle\langle I_j(x,y)\rangle},$$

1090 where $\delta I_i(x,y) = I_i(x,y) - \langle I_i(x,y)\rangle$.

1091 ACF amplitudes were corrected as described in (35) to account for the effect of the high-pass
1092 filter. A three-dimensional normal diffusion RICS fit model (5, 6) for Gaussian focal volume
1093 geometry (with particle number *N*, diffusion coefficient *D*, waist $\omega_0$, and structure parameter *S*
1094 as free fit parameters) was then fitted to both, ACFs and CCFs:

1095 $$G(\xi,\psi) = \frac{1}{N}\left(1+\frac{4D|(\xi-\xi_0)\tau_p+\psi\tau_l|}{\omega_0^2}\right)^{-1}\left(1+\frac{4D|(\xi-\xi_0)\tau_p+\psi\tau_l|}{\omega_0^2 S^2}\right)^{-1/2} exp\left(-\frac{\delta s^2((\xi-\xi_0)^2+\psi^2)}{\omega_0^2+4D|(\xi-\xi_0)\tau_p+\psi\tau_l|}\right),$$

1096 where $\tau_p$, $\tau_l$ denote the pixel dwell and line time and δs the pixel size. The free parameter $\xi_0$
1097 (starting value = 13 pixels) was used to determine which CCFs were too noisy (i.e. $\xi_0 > 4$
1098 pixels) to obtain meaningful parameters (typically in the absence of interaction). For ACF

analysis, $\xi_0$ was set to 0. To remove shot noise contributions, the correlation at zero lag time was omitted from the analysis.

From the fit amplitudes of the ACFs and CCFs, rel.cc. values were calculated:

$$rel.cc._{i,j} = max\left\{\frac{G_{i,j}(0,0)}{G_i(0,0)}, \frac{G_{i,j}(0,0)}{G_j(0,0)}\right\},$$

where $G_{i,j}(0,0)$ is the amplitude of the CCF of species $i$ and $j$, and $G_i(0,0)$ the ACF amplitude of species $i$. In the case of non-meaningful convergence of the fit to the CCFs (i.e. $\xi_0 > 4$ pixels), the rel.cc. was simply set to 0. To ensure statistical robustness of the RSICS analysis and sufficient SNR, the analysis was restricted to cells expressing all fluorophore species in comparable amounts, i.e. relative average signal intensities of less than 1:6 for all species (in all RSICS experiments). The molecular brightness of species $i$ was calculated by dividing the average count rate in the ROI by the particle number determined from the fit to the ACF: $B_i = \frac{\langle I_i(t)\rangle}{N_i}$. From this value, an estimate of the oligomeric state $\varepsilon_i$ was determined by normalizing $B_i$ by the average molecular brightness $B_{i,1}$ of the corresponding monomeric reference, and, subsequently, by the fluorescence probability $p_{f,i}$ for species $i$: $\varepsilon_i = \frac{\frac{B_i}{B_{i,1}}-1}{p_{f,i}} + 1$, as previously derived (14). The $p_f$ was calculated from the obtained molecular brightness $B_{i,2}$ of FP homo-dimers of species $i$: $p_f = \frac{B_{i,1}}{B_{i,2}} - 1$ (14).

**Triple raster image correlation spectroscopy (TRICS) analysis**

TRICS was performed using three-dimensional RSICS image stacks $I_i(x, y, t)$ detected for three species $i$. First, the spatial triple correlation function (3CF) was calculated:

$$G_{1,2,3}(\xi_1, \psi_1, \xi_2, \psi_2) = \frac{\langle \delta I_i(x,y)\delta I_j(x+\xi_1,y+\psi_1)\delta I_k(x+\xi_2,y+\psi_2)\rangle}{\langle I_i(x,y)\rangle\langle I_j(x,y)\rangle\langle I_k(x,y)\rangle},$$

where $\xi_1, \xi_2$ denote spatial lags along lines and $\psi_1, \psi_2$ along columns of the image stacks. Contributions from $\delta I$ triplets containing at least two intensity values from the same pixel

position were not included in the calculation, in order to avoid shot-noise artefacts (since all channels are detected here by the same detector). From the resulting four-dimensional matrix, a two-dimensional representation was calculated by introducing coordinates *a, b* for the effective spatial shift between signal fluctuations evaluated for the two species combinations:

$$a = ceil\left(\sqrt{{\xi_1}^2 + {\xi_2}^2}\right),$$

$$b = ceil\left(\sqrt{{\psi_1}^2 + {\psi_2}^2}\right).$$

The four-dimensional triple correlation matrix was transformed into a two-dimensional representation $G_{3C}(a,b)$ by rounding up *a* and *b* to integer values and averaging all points with the same rounded spatial shift. For example, for a 1-pixel shift along a line in one FP channel and a 1-pixel shift along a column in the third FP channel (i.e. $\xi_1 = 1, \psi_1 = 0, \xi_2 = 0, \psi_2 = 1$), *a*=*b*=1. $G_{3C}(1,1)$ also includes in its averaged value the other seven correlation values corresponding e.g. to $(\xi_1 = 0, \psi_1 = 1, \xi_2 = 1, \psi_2 = 0)$, $(\xi_1 = 1, \psi_1 = 0, \xi_2 = 0, \psi_2 = -1)$ and so on. As a further example, $G_{3C}(2,0)$ includes and averages only the two correlation values corresponding to $\psi_1 = \psi_2 = 0$ (i.e. no shift along columns) and $\xi_1 = -\xi_2 = \pm 1$ (i.e. a 1-pixel shift along a line, in opposite directions for the two channels). Note that the combinations $(\psi_1 = \psi_2 = 0, \xi_1 = \pm 2, \xi_2 = 0)$ and $(\psi_1 = \psi_2 = 0, \xi_1 = 0, \xi_2 = \pm 2)$ would also result in *a*=2 and *b*=0, but these values were not included since they refer to a correlation between identical pixel positions (e.g. $\xi_2 = 0, \psi_2 = 0$) between two FP channels and would be influenced by shot-noise artefacts (see above).

To determine the triple correlation amplitude $G_{3C}(0,0)$, the closest points (e.g. $G_{3C}(1,1)$, $G_{3C}(1,2)$, $G_{3C}(2,1)$, $G_{3C}(2,2)$, $G_{3C}(3,0)$) of the two-dimensional triple correlation were averaged, as an (slightly underestimated) approximation of the amplitude value at (0,0). Note that we chose not to include $G_{3C}(2,0)$ because this point is the average of only two possible spatial shift combinations, resulting in large statistical noise. Also, the point $G_{3C}(0,3)$ was not included since

it refers to shifts along columns (i.e. the slow scanning direction) which, in turn, are characterized by a steeper decrease in amplitude. Finally, for best visualization, $G_{3C}$ is plotted for $a$ and $b$ values ≥1 (see Fig. 7 and Appendix-figure 2).

To account for reduction of the triple correlation amplitude due to the high-pass filter, an empirical correction was applied based on simulated triple correlation amplitudes with different sizes $\Delta F$ of the moving window (see Appendix, paragraph 2 and Appendix-figure 1). Notably, applying this empirical correction to the auto- and cross-correlation amplitudes confirmed the previously introduced correction formula (see Appendix-figure 1), $G_{corr}(\xi,\psi) = \frac{\Delta F}{\Delta F - 1} G(\xi,\psi)$ (35). The triple correlation amplitude is related to the number of triple complexes $N_{3C}$ (20, 68):

$$G_{3C}(0,0) = \frac{4N_{3C}}{3N_1N_2N_3} = \frac{4N_{3C}}{3} G_1(0,0)G_2(0,0)G_3(0,0),$$

where $N_i$ is the total number of proteins detected for species $i$. In analogy to the rel.cc., a relative triple correlation rel.3C. is defined, quantifying the fraction of triple complexes relative to the total number of proteins of the species that is present in the lowest concentration:

$$rel.3C. = max\left\{\frac{N_{3C}}{N_1}, \frac{N_{3C}}{N_2}, \frac{N_{3C}}{N_3}\right\} = \frac{3}{4}\frac{G_{3C}(0,0)}{G_1(0,0)G_2(0,0)G_3(0,0)} max\{G_1(0,0), G_2(0,0), G_3(0,0)\}.$$

**Statistical Analyses**

All data are displayed as scatter dot plots indicating mean values and SDs. Sample size is given in parentheses in each graph. Statistical significance was tested using Welch's corrected two-tailed student's t-test in GraphPad Prism 7.0 (GraphPad Software) and p-values are given in figure captions.

1171 # APPENDIX

1172 ## 1. Is pair-wise cross-correlation analysis sufficient to detect ternary interactions?

1173 Generally, pair-wise cross-correlation analysis can only detect pair-wise interactions between
1174 fluorescently tagged protein species. To understand whether this analysis is sufficient to
1175 indicate the presence of hetero-trimeric protein complexes for the specific case reported in this
1176 work, we investigated brightness and rel.cc. data obtained by RSICS measurements of IAV PC
1177 proteins in more detail.

1178 For all three protein species (PA-mEYFP, PB1-mEGFP, PB2-mCherry2, referred here simply
1179 as A, B and C), normalized brightness values close to the values of FP-homo-dimers were
1180 observed in this work. As a simple approximation, we assume therefore that each species,
1181 independently of its participation in hetero-complexes, is either i) exclusively dimeric or ii)
1182 present as a well-defined mixture of monomers and homo-trimers. For the latter case, the
1183 fraction of monomers ($f_{1,i}$) and trimers ($f_{3,i}$) for each species $i$ can be calculated from the average
1184 molecular brightness $\langle\varepsilon\rangle_i$:

1185 $$f_{1,i} = \frac{1}{1+\frac{\varepsilon_{1,i}(\varepsilon_{1,i}-\langle\varepsilon\rangle_i)}{\varepsilon_{3,i}(\langle\epsilon\rangle_i-\varepsilon_{3,i})}},$$

1186 $$f_{3,i} = \frac{1}{1+\frac{\varepsilon_{3,i}(\langle\varepsilon\rangle_i-\varepsilon_{3,i})}{\varepsilon_{1,i}(\varepsilon_{1,i}-\langle\varepsilon\rangle_i)}},$$

1187 where $\varepsilon_{1,i}$ and $\varepsilon_{3,i}$ denote the molecular brightness of monomers and trimers, respectively.

1188 We then calculate the maximum rel.cc. amplitudes that can be expected in the presence of
1189 optimal pair-wise interactions, while still assuming a negligible concentration of complexes
1190 containing A, B, and C.

1191 Generally, the ACF and CCF amplitudes for multiple populations (i.e. complexes of species $i$
1192 and $j$ with variable stoichiometry) are calculated as follows (69):

1193 $$G_i(0,0) = \frac{\sum_k \varepsilon_{k,i}^2 c_k}{V_{\text{eff}}(\sum_k \varepsilon_{k,i} c_k)^2},$$

1194 $$G_{i,j}(0,0) = \frac{\sum_k \varepsilon_{k,i}\varepsilon_{k,j}c_k}{V_{\text{eff}}(\sum_k \varepsilon_{k,i}c_k)(\sum_k \varepsilon_{k,j}c_k)},$$

1195 where $\varepsilon_{k,i}$ and $\varepsilon_{k,j}$ denote the molecular brightness of population $k$ of species $i$ and $j$ (assumed
1196 here to be the same for all species), present at a concentration $c_k$ in the effective volume $V_{eff}$.
1197 For the sake of simplicity, we discuss here only two simple possible scenarios for the two
1198 mixtures discussed above (i.e. each PC protein being present exclusively as homo-dimers or as
1199 a mixture of monomers and homo-trimers), in the absence of complexes containing all three
1200 PC subunits:
1201 1) homo-dimers interacting with homo-dimers of the other species (i.e. AA-BB, AA-CC, BB-
1202 CC).
1203 2) monomers and oligomers interacting (exclusively) with monomers or oligomers of the other
1204 species (i.e. A-B, A-C, B-C, AAA-BBB, AAA-CCC, BBB-CCC).
1205 The two scenarios evaluated here correspond to configurations with the highest possible pair-
1206 wise correlations (in the absence of complexes containing A, B, and C), still compatible with
1207 an average oligomerization value of 2.
1208 For the two scenarios, we calculate ACF and CCF amplitudes according to the formulas given
1209 above, assuming the same total concentration for all species and replacing the concentrations
1210 by the derived relative fractions of monomers and oligomers. For each scenario, we determine
1211 rel.cc. values from the ratio of CCF and ACF amplitudes. Finally, we extend our calculations
1212 by considering incomplete maturation of FP tags based on the fluorescence probability $p_f$. For
1213 simplicity, we assume the same $p_f$ for each FP species, in agreement with the similar $p_f$ values
1214 of ca. 60-75% observed here for mEGFP, mEYFP and mCherry2. We use a binomial model for
1215 the relative occurrence of different subpopulations in each species (14). For example, actual
1216 trimers give rise to a fraction $f_k$ of fluorescent trimers ($k=3$), dimers ($k=2$), or monomers ($k=1$)
1217 with a relative occupancy of $f_k = \binom{3}{k} p_f^k (1-p_f)^{3-k}$ and brightness $k\varepsilon_1$.

1218 The obtained rel.cc. values for all models are given in Appendix-table 1 for $p_f=1$ or $p_f=0.7$. For
1219 comparison, we also calculated rel.cc. values of the positive control, i.e. the maximum pair-
1220 wise rel.cc. for 1:1 stoichiometry hetero-dimers (A-B/ A-C/ B-C) or 1:1:1 stoichiometry hetero-
1221 trimers (A-B-C), resulting in values of 1 (for $p_f=1$) and 0.7 (for $p_f=0.7$). Experimentally, this
1222 control would also account for suboptimal overlap of the detection volumes for each FP
1223 combination, which we neglected here for simplicity. In the absence of ternary hetero-
1224 interactions, the determined rel.cc. values are at maximum 59% of the rel.cc. of the positive
1225 control (i.e. 0.59 for $p_f=0.7$ for scenario 1). Higher normalized values (up to 1.19, see
1226 Appendix-table 1) can be obtained only in the presence of hetero-complexes involving all three
1227 PC subunits, which we calculated for comparison for the two mixtures (i.e. AA-BB-CC, or A-
1228 B-C in mixtures with AAA-BBB-CCC) and both $p_f$ values.
1229 Of note, in our experiments, rel.cc. values >0.7 (relative to the positive control) were observed
1230 for all pair-wise interactions between PC subunits (detected average pair-wise rel.cc. values
1231 normalized to the positive control were 0.71 for B-C, 0.97 for A-C, and 1.43 for A-B, see
1232 Fig.6D). As shown based on the different binding models, such high pair-wise rel.cc. values
1233 are only possible if ternary complexes are present. Thus, by combining molecular brightness
1234 and cross-correlation analysis, we conclude that PC proteins form a substantial amount of
1235 ternary complexes in the nucleus of cells.
1236

1237 **Appendix-table 1. Relative cross-correlation values (here, same for all channel combinations) for pair-wise**
1238 **or ternary interactions of three-species mixtures.** Values in brackets for $p_f=0.7$ give rel.cc. values normalized
1239 to that of the positive control (i.e. the pair-wise rel.cc. for 1:1 stoichiometry).

| **Binding model** | $p_f$**=1** | $p_f$**=0.7** |
|---|---|---|
| pair-wise interactions of dimers (e.g. AA-BB, AA-CC, BB-CC) | 0.50 | 0.41 (0.59) |
| pair-wise interactions of monomers and homo-trimers (e.g. A-B, A-C, B-C, AAA-BBB, AAA-CCC, BBB-CCC) | 0.5 | 0.40 (0.57) |
| positive control (A-B/A-C/B-C or A-B-C) | 1.0 | 0.7 (1.0) |
| ternary interactions of dimers (e.g. AA-BB-CC) | 1.0 | 0.83 (1.19) |
| ternary interactions of monomers and trimers (e.g. A-B-C, AAA-BBB-CCC) | 1.0 | 0.80 (1.14) |

1240

1241 **2. TRICS analysis of simulated three-species RICS data**

1242 To evaluate the performance of TRICS, we analyzed first simulated RICS data. We ran Monte-
1243 Carlo simulations of three-species RICS for either i) three independently diffusing species A,
1244 B, C or ii) a hetero-trimeric species (e.g. A-B-C complexes). Two-dimensional diffusion and
1245 image acquisition were simulated with the following parameters: diffusion coefficient $D$=1
1246 $\mu m^2/s$ (set to be the same for all species), $N$=1000 particles (for each species), waist $\omega_0$=0.2
1247 µm, pixel size δs=0.05 µm, pixel dwell time $\tau_p$=2 µs, 256x256 pixels, 100 frames. RICS ACFs,
1248 CCFs and the TRICS 3CF were calculated. To correct for the reduction of the triple correlation
1249 due to the high-pass filter (with filter size of $\Delta F$ frames), an empirical correction was applied.
1250 To this aim, the variance and third central moment of a series of $10^5$ random numbers, sampled
1251 from a Poissonian distribution (with mean $f_0 = 10$), were calculated within windows with
1252 variable size $\Delta F$ (Appendix-figure 1). The empirical function $f_i(\Delta F) = f_0 \left(\frac{\Delta F-1}{\Delta F}\right)^{b_i}$ was fitted
1253 to the variance ($i$=2) and third central moment ($i$=3). For the variance and third central moment,
1254 $b_2$=1.0 and $b_3$=3.4 were obtained, respectively. Thus, the reduction of variance and third central
1255 moment for a given value $\Delta F$ can be corrected using the factor $\left(\frac{\Delta F}{\Delta F-1}\right)^{b_i}$. For the variance, the
1256 determined value $b_2$ is in agreement with a previously discussed correction (35), which was
1257 used here to correct experimental ACFs and CCFs. To test whether 3CFs can be effectively
1258 corrected with the obtained $\left(\frac{\Delta F}{\Delta F-1}\right)^{b_3}$ factor, 3CFs were calculated with variable $\Delta F$ (in the
1259 range 2-16) and the amplitude values determined with or without the correction. In the latter
1260 case, fairly constant 3CF amplitudes were obtained, agreeing with the 3CF amplitude calculated
1261 without the high-pass filter (data not shown). Exemplary 3CFs for the two simulated scenarios
1262 are shown in Appendix-figure 2. As expected, the rel.3C. values are close to 100% in the case
1263 of hetero-trimers and 0% in the case of independently diffusing monomers. The slight

underestimation of the rel.3C. for hetero-trimers is likely due to the approximated interpolation of the amplitude value from only the first five points of the 3CF.

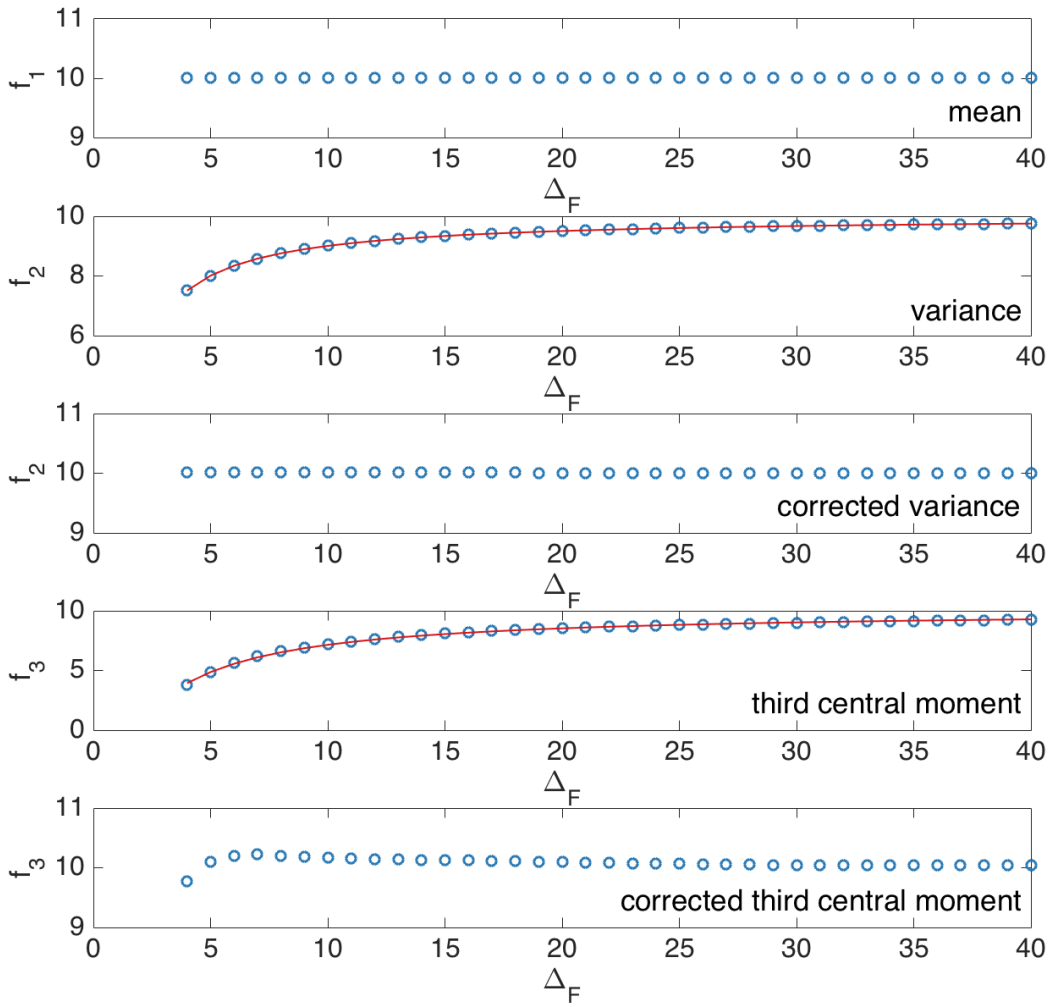


**Appendix-figure 1. Effect of high-pass filter on calculation of variance and third central moment of random numbers sampled from a Poissonian probability distribution.** Variance ($f_2$, blue circles) and third central moment ($f_3$, blue circles) where calculated with a moving average (window size $\Delta F$) for a set of $10^5$ random numbers from a Poissonian distribution with average 10. An empirical function (red solid line) of the form $f_i(\Delta F) = f_0 \left(\frac{\Delta F - 1}{\Delta F}\right)^{b_i}$ was fitted to the variance ($f_2$) and third central moment ($f_3$), and used to correct for the undersampling effect. The corresponding values after applying the empirical correction are shown as blue circles in the panels labeled as "corrected".

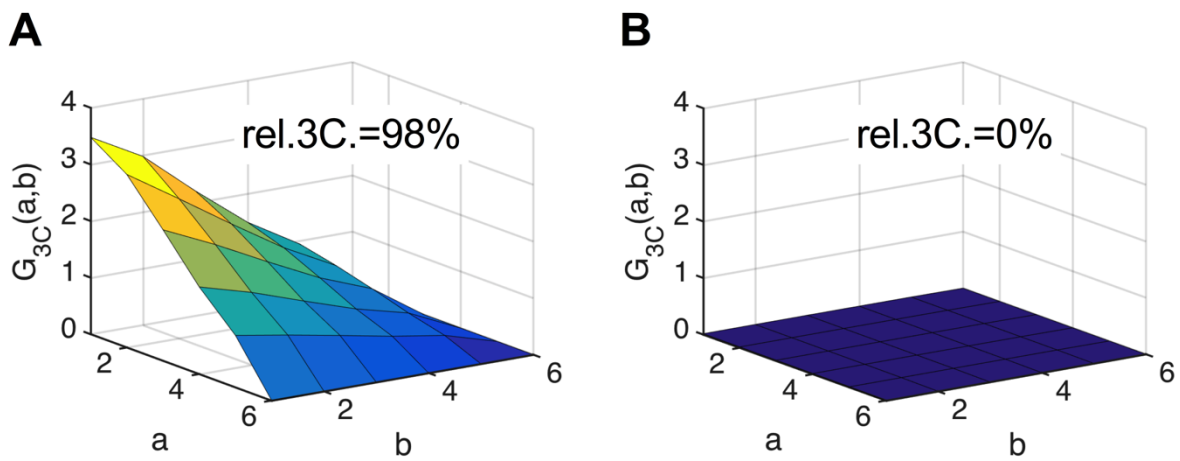


**Appendix-figure 2. TRICS analysis of simulated three-species RICS data. (A,B)** Two-dimensional representation of the 3CF calculated for simulated TRICS data (with a 4-frame high-pass filter) for (A) ternary hetero-complexes or (B) the same number of particles per species diffusing as independent monomers. From a linear interpolation of $G_{3C}$ to *(0,0)* (using the first point $G_{3C}(1,1)$ and the average of the four points $G_{3C}(1,2)$, $G_{3C}(2,1)$, $G_{3C}(2,2)$, $G_{3C}(3,0)$) an approximate value of the 3CF amplitude was determined and corrected with the correction factor discussed in paragraph 1. The obtained value and the ACF amplitude value (also corrected for the decay induced by the high-pass filter) were used to calculate the relative triple correlation value rel.3C. (given as inset).

### 3. Relative triple correlation for ternary complexes of fluorescently tagged proteins

The rel.3C. is a measure of the relative amount of ternary complexes in a system containing three fluorescently tagged protein species. Incomplete maturation or non-fluorescent photophysical states of FP tags will reduce the amount of detectable ternary complexes. To quantify the maximum rel.3C. that can be expected in an experiment, we calculate rel.3C. values for ternary complexes of i) *1:1:1* or ii) *2:2:2* stoichiometry, under the assumption that each fluorescent protein can be detected with a probability $p_f$. For simplicity, we assume the same $p_f$ and molecular brightness $\varepsilon$ for all three fluorophore species. Generally, the ACF and 3CF amplitudes for fully-formed ternary complexes (i.e. in absence of partially-formed complexes) of concentration $c$ composed of species *1*, *2* and *3* with variable stoichiometry *l:m:n* are calculated as follows (69):

$$G_1(0,0) = \frac{c\left(\sum_{i=1}^{l}(i\varepsilon)^2\binom{l}{i}p_f^i(1-p_f)^{l-i}\right)}{V_{\text{eff}}\left(c\sum_{i=1}^{l}i\varepsilon\binom{l}{i}p_f^i(1-p_f)^{l-i}\right)^2} \quad \text{(analogously } G_2(0,0),\ G_3(0,0) \text{ with upper index } m,n\text{)},$$

$$G_{3C}(0,0) = \frac{c\left(\sum_{i=1}^{l}(i\varepsilon)^2\binom{l}{i}p_f^i(1-p_f)^{l-i}\right)\left(\sum_{j=1}^{m}(j\varepsilon)^2\binom{m}{j}p_f^j(1-p_f)^{m-j}\right)\left(\sum_{k=1}^{n}(k\varepsilon)^2\binom{n}{k}p_f^k(1-p_f)^{n-k}\right)}{V_{\text{eff}}\left(c\sum_{i=1}^{l}i\varepsilon\binom{l}{i}p_f^i(1-p_f)^{l-i}\right)\left(c\sum_{j=1}^{m}j\varepsilon\binom{m}{j}p_f^j(1-p_f)^{m-j}\right)\left(c\sum_{k=1}^{n}k\varepsilon\binom{n}{k}p_f^k(1-p_f)^{n-k}\right)}.$$

1298 From these amplitudes, the rel.3C. can be calculated (see Materials and Methods in the main
1299 manuscript). We obtain rel.3C.=$p_f^2$=0.49 (1:1:1 stoichiometry) and rel.3C.=$4p_f^2/(p_f+1)^2 \approx 0.68$
1300 (2:2:2 stoichiometry) for $p_f$=0.7. Due to imperfect optical overlap, experimentally detectable
1301 rel.3C. values will be lower than these values. To estimate the fraction of ternary complexes
1302 than can be detected, we compare experimental rel.cc. values obtained for all FP combinations
1303 on a positive control (FP hetero-trimers) in pair-wise cross-correlation analysis with the
1304 expected value of rel.cc.=0.7 for $p_f$=0.7 (see paragraph 1). The average rel.cc. value of 0.65
1305 detected for mEGFP and mEYFP signal (see Fig.6D of main manuscript) was close to the
1306 expected value, hence, almost all complexes containing fluorescent mEGFP and mEYFP were
1307 detectable. On the other hand, rel.cc. values for mEGFP and mCherry2 (0.48)/ mEYFP and
1308 mCherry2 (0.53) were ca.70% of the expected value (Fig.6D). Hence, we estimate that ca. 70%
1309 of complexes carrying an mCherry2 tag and an mEGFP or mEYFP tag are detectable, due to
1310 non-optimal overlap of excitation/detection volumes. We can therefore assume that for the case
1311 of ternary complexes, ca.70% of all fully fluorescent ternary complexes that are present in the
1312 sample are optically detectable. The expected experimental rel.3C. values are thus
1313 approximately 0.34 and 0.48 for complete binding in 1:1:1 and 2:2:2 stoichiometry,
1314 respectively.
1315
1316

1317 **ACKNOWLEDGEMENTS**

1318 This work was financed by the DFG 254850309 grant to S.C. The LSM 880 instrumentation
1319 was funded by the German Research Foundation (DFG) grant INST 336/114-1 FUGG. The
1320 authors kindly thank Madlen Luckner for providing the plasmids for PA-mEYFP, PB1-mEGFP
1321 and PB2-mCherry2 expression, Thorsten Wohland for providing the PMT-mApple plasmid and
1322 Jelle Hendrix for fruitful discussion.

1323 **REFERENCES**


1324 1. Jameson, D.M., J.A. Ross, and J.P. Albanesi. 2009. Fluorescence
1325 fluctuation spectroscopy: ushering in a new age of enlightenment for
1326 cellular dynamics. *Biophys. Rev.* 1:105–118.

1327 2. Weidemann, T., J. Mücksch, and P. Schwille. 2014. Fluorescence
1328 fluctuation microscopy: a diversified arsenal of methods to investigate
1329 molecular dynamics inside cells. *Curr. Opin. Struct. Biol.* 28:69–76.

1330 3. Petazzi, R.A., A.K. Aji, and S. Chiantia. 2020. Fluorescence microscopy
1331 methods for the study of protein oligomerization. In: Progress in
1332 Molecular Biology and Translational Science. Elsevier B.V. pp. 1–41.

1333 4. Schwille, P., F.J. Meyer-Almes, and R. Rigler. 1997. Dual-color
1334 fluorescence cross-correlation spectroscopy for multicomponent
1335 diffusional analysis in solution. *Biophys. J.* 72:1878–1886.

1336 5. Digman, M.A., C.M. Brown, P. Sengupta, P.W. Wiseman, A.R. Horwitz,
1337 and E. Gratton. 2005. Measuring fast dynamics in solutions and cells with
1338 a laser scanning microscope. *Biophys. J.* 89:1317–27.

1339 6. Digman, M.A., P.W. Wiseman, A.R. Horwitz, and E. Gratton. 2009.
1340 Detecting protein complexes in living cells from laser scanning confocal
1341 image sequences by the cross correlation raster image spectroscopy
1342 method. *Biophys. J.* 96:707–16.

1343 7. Digman, M. a, R. Dalal, A.F. Horwitz, and E. Gratton. 2008. Mapping the
1344 number of molecules and brightness in the laser scanning microscope.

1345 *Biophys. J.* 94:2320–2332.

1346 8. Digman, M.A., P.W. Wiseman, C. Choi, A.R. Horwitz, and E. Gratton.
1347 2009. Stoichiometry of molecular complexes at adhesions in living cells.
1348 *Proc. Natl. Acad. Sci. U. S. A.* 106:2170–2175.

1349 9. Krieger, J.W., A.P. Singh, N. Bag, C.S. Garbe, T.E. Saunders, J.
1350 Langowski, and T. Wohland. 2015. Imaging fluorescence (cross-)
1351 correlation spectroscopy in live cells and organisms. *Nat. Protoc.*
1352 10:1948–1974.

1353 10. Magde, D., E. Elson, and W.W. Webb. 1972. Thermodynamic
1354 Fluctuations in a Reacting System - Measurement by Fluorescence
1355 Correlation Spectroscopy. *Phys. Rev. Lett.* 29:705–708.

1356 11. Ries, J., and P. Schwille. 2006. Studying Slow Membrane Dynamics with
1357 Continuous Wave Scanning Fluorescence Correlation Spectroscopy.
1358 *Biophys. J.* 91:1915–1924.

1359 12. Ries, J., S.R. Yu, M. Burkhardt, M. Brand, and P. Schwille. 2009. Modular
1360 scanning FCS quantifies receptor-ligand interactions in living multicellular
1361 organisms. *Nat. Methods*. 6.

1362 13. Dunsing, V., M. Mayer, F. Liebsch, G. Multhaup, and S. Chiantia. 2017.
1363 Direct evidence of amyloid precursor-like protein 1 trans interactions in
1364 cell-cell adhesion platforms investigated via fluorescence fluctuation
1365 spectroscopy. *Mol. Biol. Cell*. 28:3609–3620.

1366 14. Dunsing, V., M. Luckner, B. Zühlke, R.A. Petazzi, A. Herrmann, and S.

1367 Chiantia. 2018. Optimal fluorescent protein tags for quantifying protein
1368 oligomerization in living cells. *Sci. Rep.* 8:10634.
1369 15. Galperin, E., V. V Verkhusha, and A. Sorkin. 2004. Three-chromophore
1370 FRET microscopy to analyze multiprotein interactions in living cells. *Nat.*
1371 *Methods*. 1:209–217.
1372 16. Sun, Y., H. Wallrabe, C.F. Booker, R.N. Day, and A. Periasamy. 2010.
1373 Three-Color Spectral FRET Microscopy Localizes Three Interacting
1374 Proteins in Living Cells. *Biophys. J.* 99:1274–1283.
1375 17. Hur, K.H., Y. Chen, and J.D. Mueller. 2016. Characterization of Ternary
1376 Protein Systems in Vivo with Tricolor Heterospecies Partition Analysis.
1377 *Biophys. J.* 110:1158–1167.
1378 18. Burkhardt, M., K.G. Heinze, and P. Schwille. 2005. Four-color
1379 fluorescence correlation spectroscopy realized in a grating-based detection
1380 platform. *Opt. Lett.* 30:2266.
1381 19. Hwang, L.C., M. Gösch, T. Lasser, and T. Wohland. 2006. Simultaneous
1382 Multicolor Fluorescence Cross-Correlation Spectroscopy to Detect Higher
1383 Order Molecular Interactions Using Single Wavelength Laser Excitation.
1384 *Biophys. J.* 91:715–727.
1385 20. Heinze, K.G., M. Jahnz, and P. Schwille. 2004. Triple-Color Coincidence
1386 Analysis: One Step Further in Following Higher Order Molecular
1387 Complex Formation. *Biophys. J.* 86:506–516.
1388 21. Ridgeway, W.K., D.P. Millar, and J.R. Williamson. 2012. Quantitation of

1389 ten 30S ribosomal assembly intermediates using fluorescence triple
1390 correlation spectroscopy. *Proc. Natl. Acad. Sci. U. S. A.* 109:13614–
1391 13619.
1392 22. Benda, A., P. Kapusta, M. Hof, and K. Gaus. 2014. Fluorescence spectral
1393 correlation spectroscopy (FSCS) for probes with highly overlapping
1394 emission spectra. *Opt. Express*. 22:2973.
1395 23. Böhmer, M., M. Wahl, H.J. Rahn, R. Erdmann, and J. Enderlein. 2002.
1396 Time-resolved fluorescence correlation spectroscopy. *Chem. Phys. Lett.*
1397 353:439–445.
1398 24. Kapusta, P., M. Wahl, A. Benda, M. Hof, and J. Enderlein. 2007.
1399 Fluorescence lifetime correlation spectroscopy. *J. Fluoresc.* 17:43–48.
1400 25. Ghosh, A., N. Karedla, J.C. Thiele, I. Gregor, and J. Enderlein. 2018.
1401 Fluorescence lifetime correlation spectroscopy: Basics and applications.
1402 *Methods*. 140–141:32–39.
1403 26. Padilla-Parra, S., N. Audugé, M. Coppey-Moisan, and M. Tramier. 2011.
1404 Dual-color fluorescence lifetime correlation spectroscopy to quantify
1405 protein-protein interactions in live cell. *Microsc. Res. Tech.* 74:788–793.
1406 27. Schrimpf, W., V. Lemmens, N. Smisdom, M. Ameloot, D.C. Lamb, and J.
1407 Hendrix. 2018. Crosstalk-free multicolor RICS using spectral weighting.
1408 *Methods*. 140–141:97–111.
1409 28. Štefl, M., K. Herbst, M. Rübsam, A. Benda, and M. Knop. 2020. Single-
1410 Color Fluorescence Lifetime Cross-Correlation Spectroscopy In Vivo.

1411 *Biophys. J.* 119:1359–1370.

1412 29. Foo, Y.H., N. Naredi-Rainer, D.C. Lamb, S. Ahmed, and T. Wohland.
1413 2012. Factors affecting the quantification of biomolecular interactions by
1414 fluorescence cross-correlation spectroscopy. *Biophys. J.* 102:1174–83.

1415 30. Foust, D.J., A.G. Godin, A. Ustione, P.W. Wiseman, and D.W. Piston.
1416 2019. Two-Color Spatial Cumulant Analysis Detects Heteromeric
1417 Interactions between Membrane Proteins. *Biophys. J.* 117:1764–1777.

1418 31. Florin, L., and T. Lang. 2018. Tetraspanin assemblies in virus infection.
1419 *Front. Immunol.* 9:1140.

1420 32. Hantak, M.P., E. Qing, J.T. Earnest, and T. Gallagher. 2018. Tetraspanins:
1421 Architects of Viral Entry and Exit Platforms. *J. Virol.* 93.

1422 33. Dahmane, S., C. Doucet, A. Le Gall, C. Chamontin, P. Dosset, F. Murcy,
1423 L. Fernandez, D. Salas, E. Rubinstein, M. Mougel, M. Nollmann, and P.E.
1424 Milhiet. 2019. Nanoscale organization of tetraspanins during HIV-1
1425 budding by correlative dSTORM/AFM. *Nanoscale*. 11:6036–6044.

1426 34. Beale, R., H. Wise, A. Stuart, B.J. Ravenhill, P. Digard, and F. Randow.
1427 2014. A LC3-interacting motif in the influenza A virus M2 protein is
1428 required to subvert autophagy and maintain virion stability. *Cell Host*
1429 *Microbe*. 15:239–247.

1430 35. Hendrix, J., T. Dekens, W. Schrimpf, and D.C. Lamb. 2016. Arbitrary-
1431 Region Raster Image Correlation Spectroscopy. *Biophys. J.* 111:1785–
1432 1796.

1433 36. Huet, S., S. V Avilov, L. Ferbitz, N. Daigle, S. Cusack, and J. Ellenberg.
1434 2010. Nuclear import and assembly of influenza A virus RNA polymerase
1435 studied in live cells by fluorescence cross-correlation spectroscopy. *J.*
1436 *Virol.* 84:1254–64.
1437 37. Kaliszewski, M.J., X. Shi, Y. Hou, R. Lingerak, S. Kim, P. Mallory, and
1438 A.W. Smith. 2018. Quantifying membrane protein oligomerization with
1439 fluorescence cross-correlation spectroscopy. *Methods*. 140–141:40–51.
1440 38. Shi, X., H.F. Yong, T. Sudhaharan, S.W. Chong, V. Korzh, S. Ahmed, and
1441 T. Wohland. 2009. Determination of dissociation constants in living
1442 zebrafish embryos with single wavelength fluorescence cross-correlation
1443 spectroscopy. *Biophys. J.* 97:678–686.
1444 39. Sankaran, J., H. Balasubramanian, W.H. Tang, X.W. Ng, A. Röllin, and T.
1445 Wohland. 2020. SRRF 'n' TIRF - FCS: Simultaneous spatiotemporal
1446 super-resolution microscopy. *bioRxiv*. 2020.02.26.965905.
1447 40. Cranfill, P.J., B.R. Sell, M.A. Baird, J.R. Allen, Z. Lavagnino, H.M. de
1448 Gruiter, G.-J. Kremers, M.W. Davidson, A. Ustione, and D.W. Piston.
1449 2016. Quantitative assessment of fluorescent proteins. *Nat. Methods*.
1450 13:557–562.
1451 41. Hendrix, J., C. Flors, P. Dedecker, J. Hofkens, and Y. Engelborghs. 2008.
1452 Dark states in monomeric red fluorescent proteins studied by fluorescence
1453 correlation and single molecule spectroscopy. *Biophys. J.* 94:4103–13.
1454 42. Bacia, K., Z. Petrášek, and P. Schwille. 2012. Correcting for spectral

1455 cross-talk in dual-color fluorescence cross-correlation spectroscopy.
1456 *ChemPhysChem*. 13:1221–1231.
1457 43. Müller, B.K., E. Zaychikov, C. Bräuchle, and D.C. Lamb. 2005. Pulsed
1458 Interleaved Excitation. *Biophys. J.* 89:3508–3522.
1459 44. Hendrix, J., W. Schrimpf, M. Höller, and D.C. Lamb. 2013. Pulsed
1460 Interleaved Excitation Fluctuation Imaging. *Biophys. J.* 105:848–861.
1461 45. Eckert, A.F., P. Gao, J. Wesslowski, X. Wang, J. Rath, K. Nienhaus, G.
1462 Davidson, and G.U. Nienhaus. 2020. Measuring ligand-cell surface
1463 receptor affinities with axial line-scanning fluorescence correlation
1464 spectroscopy. *Elife*. 9:1–92.
1465 46. Claridge, J.K., F. Mohd-Kipli, A. Florea, T. Gate, and J.R. Schnell. 2020.
1466 pH-dependent secondary structure propensity of the influenza A virus M2
1467 cytoplasmic tail. *Biomol. NMR Assign.* 14:157–161.
1468 47. Shaw, M.L., K.L. Stone, C.M. Colangelo, E.E. Gulcicek, and P. Palese.
1469 2008. Cellular Proteins in Influenza Virus Particles. *PLoS Pathog.*
1470 4:e1000085.
1471 48. Hutchinson, E.C., P.D. Charles, S.S. Hester, B. Thomas, D. Trudgian, M.
1472 Martínez-Alonso, and E. Fodor. 2014. Conserved and host-specific
1473 features of influenza virion architecture. *Nat. Commun.* 5:1–11.
1474 49. Hilsch, M., B. Goldenbogen, C. Sieben, C.T. Höfer, J.P. Rabe, E. Klipp,
1475 A. Herrmann, and S. Chiantia. 2014. Influenza A Matrix Protein M1
1476 Multimerizes upon Binding to Lipid Membranes. *Biophys. J.* 107:912–

1477 923.

1478 50. Bobone, S., M. Hilsch, J. Storm, V. Dunsing, A. Herrmann, and S.
1479 Chiantia. 2017. Phosphatidylserine lateral organization influences the
1480 interaction of influenza virus matrix protein 1 with lipid membranes. *J.*
1481 *Virol.* 91.

1482 51. Rossman, J.S., and R.A. Lamb. 2011. Influenza virus assembly and
1483 budding. *Virology*. 411:229–236.

1484 52. Fan, H., A.P. Walker, L. Carrique, J.R. Keown, I. Serna Martin, D. Karia,
1485 J. Sharps, N. Hengrung, E. Pardon, J. Steyaert, J.M. Grimes, and E. Fodor.
1486 2019. Structures of influenza A virus RNA polymerase offer insight into
1487 viral genome replication. *Nature*. 573:287–290.

1488 53. Jorba, N., E. Area, and J. Ortín. 2008. Oligomerization of the influenza
1489 virus polymerase complex in vivo. *J. Gen. Virol.* 89:520–524.

1490 54. Nilsson-Payant, B.E., J. Sharps, N. Hengrung, and E. Fodor. 2018. The
1491 Surface-Exposed PA 51-72 -Loop of the Influenza A Virus Polymerase Is
1492 Required for Viral Genome Replication . *J. Virol.* 92.

1493 55. Chen, K.-Y., E. Dos Santos Afonso, V. Enouf, C. Isel, and N. Naffakh.
1494 2019. Influenza virus polymerase subunits co-evolve to ensure proper
1495 levels of dimerization of the heterotrimer. *PLOS Pathog.* 15:e1008034.

1496 56. Ridgeway, W.K., D.P. Millar, and J.R. Williamson. 2012. The
1497 Spectroscopic Basis of Fluorescence Triple Correlation Spectroscopy. *J.*
1498 *Phys. Chem. B*. 116:1908–1919.

1499 57. Massari, S., J. Desantis, M.G. Nizi, V. Cecchetti, and O. Tabarrini. 2020.
1500 Inhibition of Influenza Virus Polymerase by Interfering with Its Protein–
1501 Protein Interactions. *ACS Infect. Dis.* acsinfecdis.0c00552.
1502 58. Ciccotosto, G.D., N. Kozer, T.T.Y. Chow, J.W.M. Chon, and A.H.A.
1503 Clayton. 2013. Aggregation Distributions on Cells Determined by
1504 Photobleaching Image Correlation Spectroscopy. *Biophys. J.* 104:1056–
1505 1064.
1506 59. Huang, L., D. Pike, D.E. Sleat, V. Nanda, and P. Lobel. 2014. Potential
1507 Pitfalls and Solutions for Use of Fluorescent Fusion Proteins to Study the
1508 Lysosome. *PLoS One*. 9:e88893.
1509 60. Işbilir, A., R. Serfling, J. Möller, R. Thomas, C. De Faveri, U. Zabel, M.
1510 Scarselli, A.G. Beck-Sickinger, A. Bock, I. Coin, M.J. Lohse, and P.
1511 Annibale. 2021. Determination of G-protein–coupled receptor
1512 oligomerization by molecular brightness analyses in single cells. *Nat.*
1513 *Protoc. 2021 163*. 16:1419–1451.
1514 61. Kimura, S., T. Noda, and T. Yoshimori. 2007. Dissection of the
1515 autophagosome maturation process by a novel reporter protein, tandem
1516 fluorescent-tagged LC3. *Autophagy*. 3:452–460.
1517 62. Dunsing, V., and S. Chiantia. 2021. SpectralFFS. *GitHub.*
1518 *https://github.com/VaDu8989/SpectralFFS*. 8942980.
1519 63. Dunsing, V., and S. Chiantia. 2018. A Fluorescence Fluctuation
1520 Spectroscopy Assay of Protein-Protein Interactions at Cell-Cell Contacts.

1521 *J. Vis. Exp.* e58582.

1522 64. Ries, J., S. Chiantia, and P. Schwille. 2009. Accurate Determination of
1523 Membrane Dynamics with Line-Scan FCS. *Biophys. J.* 96:1999–2008.

1524 65. Wohland, T., R. Rigler, and H. Vogel. 2001. The standard deviation in
1525 fluorescence correlation spectroscopy. *Biophys. J.* 80:2987–99.

1526 66. Ziegler, M., K. Yserentant, V. Middel, V. Dunsing, A. Gralak, K. Pakari,
1527 J. Bargstedt, C. Kern, S. Chiantia, U. Strähle, D.-P. Herten, and R.
1528 Wombacher. 2020. A chemical strategy to control protein networks in
1529 vivo. *bioRxiv*. 2020.04.08.031427.

1530 67. Linkert, M., C.T. Rueden, C. Allan, J.-M. Burel, W. Moore, A. Patterson,
1531 B. Loranger, J. Moore, C. Neves, D. MacDonald, A. Tarkowska, C. Sticco,
1532 E. Hill, M. Rossner, K.W. Eliceiri, and J.R. Swedlow. 2010. Metadata
1533 matters: access to image data in the real world. *J. Cell Biol.* 189:777–782.

1534 68. Palmer, A.G., and N.L. Thompson. 1987. Molecular aggregation
1535 characterized by high order autocorrelation in fluorescence correlation
1536 spectroscopy. *Biophys. J.* 52:257–270.

1537 69. Kim, S.A., K.G. Heinze, K. Bacia, M.N. Waxham, and P. Schwille. 2005.
1538 Two-Photon Cross-Correlation Analysis of Intracellular Reactions with
1539 Variable Stoichiometry. *Biophys. J.* 88:4319–4336.

1540

1541